J. Fluid Mech. (2006), *vol.* 565, *pp.* 135–169. © 2006 Cambridge University Press
doi:10.1017/S0022112006000930 Printed in the United Kingdom

Large-eddy simulation of shock-wave/turbulent-boundary-layer interaction

By MAXIM S. LOGINOV[1,2], NIKOLAUS A. ADAMS[1] AND ALEXANDER A. ZHELTOVODOV[2]

[1]Institute of Aerodynamics, Technische Universität München, D-85747 Garching, Germany
[2]Institute of Theoretical and Applied Mechanics RAS SB, Novosibirsk 630090, Russia

(Received 4 July 2005 and in revised form 23 February 2006)

Well-resolved large-eddy simulations (LES) are performed in order to investigate flow phenomena and turbulence structure of the boundary layer along a supersonic compression ramp. The numerical simulations directly reproduce an available experimental result. The compression ramp has a deflection angle of $\beta = 25^\circ$. The mean free-stream Mach number is $M_\infty = 2.95$. The Reynolds number based on the incoming boundary-layer thickness is $Re_{\delta_0} = 63\,560$ in accordance with the reference experiment. These simulations overcome deficiencies of earlier direct numerical simulations (DNS) and LES in terms of ramp-deflection angle, Reynolds number and spanwise size of the computational domain which is required for capturing the essential flow phenomena. The filtered conservation equations for mass, momentum and energy are solved with a high-order finite-difference scheme. The effect of subgrid scales is modelled by the approximate deconvolution model. About 18.5×10^6 grid points are used for discretizing the computational domain. To obtain mean flow and turbulence structure the flow is sampled 1272 times over 703 characteristic time scales of the incoming boundary layer. Statistical data are computed from these samples. An analysis of the data shows good agreement with the experiment in terms of mean quantities such as shock position, separation and reattachment location, skin-friction and surface-pressure distributions, and turbulence structure. The computational data confirm theoretical and experimental results on fluctuation amplification across the interaction region. In the wake of the main shock a shedding of shocklets is observed. The temporal behaviour of the coupled shock–separation system agrees well with experimental data. Unlike previous DNS the present simulation data provide indications of a large-scale shock motion. Also, evidence for the existence of three-dimensional large-scale streamwise structures, commonly referred to as Görtler-like vortices, is found.

1. Introduction

For supersonic flows the interaction of turbulent boundary layers with shocks and rarefaction waves is one of the most prevalent phenomena governing the overall flow structure. A striking example for the significance of a proper engineering prediction of shock-wave/turbulent-boundary-layer interaction (SWTBLI) is provided by the side-load phenomenon in rocket nozzles (e.g. Hagemann, Frey & Koschel 2002) which is responsible for numerous, even recent, design failures. Research on

https://doi.org/10.1017/S0022112006000930 Published online by Cambridge University Press

SWTBLI commonly employs a range of canonical flow configurations with increasing complexity. Among the canonical configurations considered are impinging normal shocks, oblique-shock reflections, compression ramps and one and two fins mounted on a flat plate. For a detailed survey of the current knowledge on SWTBLI, mainly drawn from experiments, refer to Delery & Marvin (1986), Settles & Dolling (1990), Smits & Dussauge (1996), Zheltovodov (1996), Andreopoulos, Agui & Briassulis (2000) and Dolling (2001). As pointed out by Dolling (1998, 2001) and confirmed by more recent comprehensive analyses (Knight *et al.* 2003) the numerical prediction of SWTBLI by statistical turbulence modelling is still unsatisfactory. For situations with shock-induced flow separation computational results employing Reynolds-averaged turbulence modelling exhibit a large scatter of predicted separation lengths for various geometrical configurations. Although numerous computations based on the Reynolds-averaged Navier–Stokes equations (RANS) have been performed, currently only weak and moderate interactions, characterized by low supersonic Mach number or small flow deflection angles, can be predicted by RANS computations without specific *a posteriori* adjustment of turbulence models. For strong interactions, the results of RANS computations generally show a significant disagreement with experimental data in terms of surface pressure, skin friction, and heat transfer distributions. Furthermore, these approaches turn out to be unable to predict the unsteadiness of the shock system, which is, however, a very important feature of SWTBLI. Comprehensive summaries of the current status of computational fluid dynamics (CFD) for the prediction of SWTBLI are given by Zheltovodov *et al.* (1992), Zheltovodov (1996), and Knight & Degrez (1998).

A main deficiency of RANS approaches is that for unsteady flows, statistical turbulence modelling can be expected to reproduce the proper temporal mean-flow behaviour only if mean-flow time scales and fluctuation time scales are separated so that standard assumptions involved in turbulence modeling can be applied. This is not the case for SWTBLI. Alternatives to RANS are the large-eddy-simulation (LES) and direct numerical simulations (DNS) approaches. DNS recovers the entire temporal and spatial flow information. Since all relevant flow scales need to be resolved DNS is limited essentially by the available computer power. In practice, only rather small Reynolds numbers and narrow computational domains can be considered. The range of flow parameters where most experimental data are available cannot be reached. Spatial and temporal resolution requirements can be lowered by employing LES at the expense of modelling the effect of discarded scales. For LES, evolution equations for the low-pass filtered solution are solved. The instantaneous interaction of these so-called resolved scales with the remainder range of scales needs to be modelled. For a comprehensive account of current LES refer to the textbook of Sagaut (2002). Nevertheless, LES maintains the main advantages of DNS, namely providing the full spatial and temporal flow information down to the smallest resolved scales. Based on recent advances in modeling and computing, LES nowadays can be considered as the most appropriate numerical tool for the analysis of complex unsteady transitional and turbulent flows. However, as pointed out by Knight *et al.* (2003) and Zheltovodov (2004), even LES predictions need to be interpreted with care. For this reason in this paper a direct comparison between an available experiment and an LES employing the approximate deconvolution model Stolz, Adams & Kleiser (2001*a*) is performed.

Engine inlets as well as some other elements of supersonic planes often have successive forward- and backward-facing ramps, so that generic compression–decompression and decompression–compression ramps configurations are also investigated. Seminal contributions on compression-corner flows have been made

https://doi.org/10.1017/S0022112006000930 Published online by Cambridge University Press

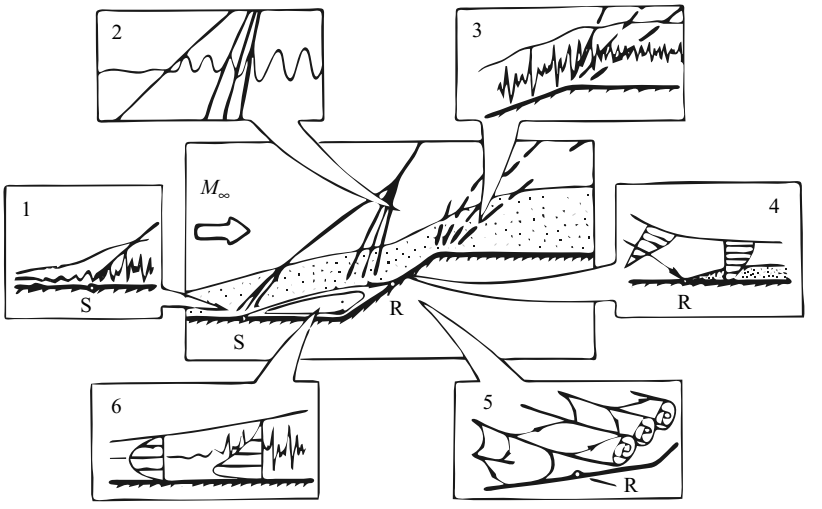


FIGURE 1. Important flow phenomena in compression ramp flows (for explanations see text).

by Settles, Fitzpatrick & Bogdonoff (1979), Dolling & Murphy (1983), and Smits & Muck (1987). A compilation of a large range of available experimental data is provided by Settles & Dodson (1994). Most of the current insight and knowledge about compression-ramp flows is drawn from experimental work, and we will not repeating the above reviews here. Essential flow phenomena for compression–decompression ramps are sketched in figure 1, following Zheltovodov (1991). The undisturbed incoming turbulent boundary layer is deflected at the compression corner. The resulting compression shock penetrates the boundary layer where the penetration depth depends on the local Reynolds number Adamson & Messiter (1980). For sufficiently large deflection angles the rapid compression within the boundary layer results in a region of mean-flow separation near the compression corner. The separation region is contained by a detached shear layer which reattaches at the deflected part of the compression ramp. A λ-shock system is generated near the separation region. The forward foot of the λ-shock originates from the region of flow separation, and the rearward foot from the region of flow reattachment. Further downstream, the reattached boundary layer reaches the decompression ramp and passes through the Prandtl–Meyer expansion. Even further downstream, the boundary layer relaxes again towards a developed zero-pressure-gradient boundary layer.

In figure 1 separation and reattachment lines are indicated by S and R, respectively. Turbulence is amplified by interaction with a rapid compression within the boundary layer (inset 1) and by direct interaction with the shock in the external flow, inset 2. Note also that the shock foots spread out towards the wall due to reduced local Mach number and to turbulent diffusion. Inset 3 points to the damping of turbulent fluctuation by the interaction with the expansion wave at the expansion corner. After reattachment at the deflected part of the compression ramp a turbulent boundary layer is re-established, inset 4. Experimental results support the existence of pairs of large counter-rotating streamwise vortices in the reattachment region as well as in the reverse flow of the separation zone, inset 5. Within the area of flow separation the reverse mean flow has the character of a wall jet which exhibits indications of relaminarization, inset 6.

https://doi.org/10.1017/S0022112006000930 Published online by Cambridge University Press

Zheltovodov (2004) and Knight *et al.* (2003) provide extensive comparisons of RANS and LES, applied to supersonic compression ramps. Probably the first attempt at an LES for compression-ramp flow was made by Hunt & Nixon (1995), who qualify their simulation as a very large-eddy simulation. The results show some agreement with the experiment of Dolling & Murphy (1983), e.g. in terms of the shock-motion frequency. For a weak interaction at a free-stream Mach number of $M_\infty = 3$ and a ramp deflection angle of $\beta = 8^\circ$ no mean-flow separation was found in the LES of Urbin, Knight & Zheltovodov (1999), Kannepalli, Arunajatesan & Dash (2002), and El-Askary, Schröder & Meinke (2003), although instantaneous reverse flow regions may exist. A thin separation zone was observed in the DNS of Adams (2000) at $M_\infty = 3, \beta = 18^\circ$. No large-scale shock motion (LSSM) was found. The observed small-scale shock motion has a dominant frequency which is close to the inverse characteristic time scale of bursting events within the incoming boundary layer. An instantaneous Schlieren-type visualization exhibits compression waves shed by the main compression shock above the separated shear layer and downstream of the interaction. These DNS results were confirmed by the LES of Stolz *et al.* (2001*a*) where the approximate deconvolution model (ADM) was employed for subgrid-scale (SGS) modelling.

The same free-stream flow parameters as in Adams (2000) were considered by Rizzetta, Visbal & Gaitonde (2001) and El-Askary *et al.* (2003). Computations without an SGS model agreed with LES with a Smagorinsky model and with a dynamic model at the same resolution, indicating that the effect of the employed SGS model was negligible. No agreement was found with the results of Adams (2000) in terms of skin-friction and surface-pressure distributions in the interaction area. Aside from the modelling issues, the main reason for this disagreement is that the incoming boundary layers were different. A case with a strong interaction was studied by Urbin *et al.* (2000), Yan *et al.* (2000) and Yan, Knight & Zheltovodov (2001) at $M_\infty = 3$ and $\beta = 25^\circ$. A range of deflection angles $\beta = 8^\circ, 16^\circ, 20^\circ, 24^\circ$, corresponding to experiments of Smits & Muck (1987), Dolling & Murphy (1983) and data of Settles & Dodson (1991), was investigated by Rizzetta & Visbal (2002). The latter case of $\beta = 24^\circ$ was also considered by Kannepalli *et al.* (2002). However, for all these computations the momentum-thickness Reynolds number of the incoming boundary layer was about one to two orders of magnitude smaller than for the experiments. For none of these computations was a developed pressure plateau near the corner observed, a result which is typical for low Reynolds numbers. Also the separation length was not reproduced correctly. No LSSM was found and the temporal evolution of the shock-separation system, in terms of the surface-pressure intermittency, exhibits quantitative differences from the experiments. Recently Wu *et al.* (2005*a*), Wu, Taylor & Martin (2005*b*) and Wu & Martin (2006) presented preliminary results for a DNS of a 24°-compression corner at a free-stream Mach number $M = 2.9$ and an incoming-boundary-layer momentum-thickness Reynolds number of $Re_\theta = 2900$, corroborating the above findings. So far there is to our knowledge no successful direct comparison with a compression-ramp experiment.

For some simulations the separation length agrees with experiment although the experimental Reynolds number is much larger. This contradicts the dependence of the separation length on Reynolds number as reported by Knight *et al.* (2003). Most of the currently available analysis is restricted to spanwise-averaged flow data and a detailed investigation of the flow structure is not available. An open question is the existence of large-scale streamwise structures in the reattaching flow and their origin. Experimental oil-flow patterns of Zheltovodov, Schülein & Yakovlev (1983)

https://doi.org/10.1017/S0022112006000930 Published online by Cambridge University Press

and Lüdeke, Radespiel & Schülein (2004) suggest the presence of pairwise counter-rotating vortices in the reverse flow of the separation zone and near reattachment. For a laminar interaction Comte & David (1996) found Görtler-like vortices for an LES of the boundary layer along a generic body–flap configuration at $Re_{\delta_0} \approx 840$, where δ_0 is the incoming boundary-layer thickness. It was shown that these vortices have a strong effect on local skin friction and heat transfer.

The objective of the numerical investigation presented in this paper is a direct comparison with an available experiment, along with a detailed investigation of the instantaneous and the averaged flow structure. For this purpose all flow parameters and the flow geometry are matched to an available experiment of Zheltovodov *et al.* (1983) and Zheltovodov & Yakovlev (1986). The experimental data are available in tabulated form and described in detail by Zheltovodov *et al.* (1990). Additional experiments providing surface skin friction measurements are available for the same geometry (Borisov *et al.* 1993). The free-stream Mach number is $M_\infty = 2.95$, the Reynolds number based on the incoming boundary-layer thickness is $Re_{\delta_0} = 63560$, and the ramp deflection angle is $\beta = 25^\circ$. In the following we refer to the experiment at such conditions as the 'reference experiment'. Additional experimental data at $M = 2.9$ and $Re_{\delta_0} = 144000$ for the same geometry will be used and referred to as 'higher-Reynolds-number experiment'. By matching directly the experimental parameters, the prediction quality of the SGS model employed can be assessed without further assumptions. Preliminary results based on the analysis of limited statistical data were considered by Loginov, Adams & Zheltovodov (2004*a*, *b*). In this report the entire set of data is used. Given a successful validation, the computational results will provide a reliable source for further analysis. Whereas the reference experiment is on an compression–decompression ramp configuration, in this paper only the compression ramp is considered and compared with the experiment. The reason for splitting the problem into two parts is twofold. First, the estimated computational cost of well-resolved LES for the full configuration is large for completing the computations in reasonable time. Second, the compression-corner interaction is sufficiently complex to justify a separate investigation. The subsequent downstream interaction of the reattached boundary layer with the Prandtl–Meyer expansion is the subject of an ongoing study.

In § 2 we provide the problem formulation and give a brief summary of the simulation method, which is essentially the same as in Stolz *et al.* (2001*a*). A precursor simulation for the turbulent boundary layer along a flat plate was used to provide inflow data for the compression ramp. Results for this precursor simulation are summarized in § 3. The main subject of this paper is the analysis of the compression-corner flow in § 4. The last section, § 5, gives a summary and final conclusions.

2. Problem formulation and simulation method

A generalized-coordinate formulation of the compressible Navier–Stokes equations (NSE) in conservation form is employed. The NSE are written in the Cartesian (x_1, x_2, x_3) physical space, using a transformation to computational space (ξ_1, ξ_2, ξ_3) as detailed by Adams (1998). The computational-space coordinates are orthogonal and normalized, where ξ_1 corresponds to the streamwise direction, ξ_2 to the spanwise direction and ξ_3 to the wall-normal direction. Note that the lines $\xi_1 = \text{const}$ and $\xi_3 = \text{const}$ are non-orthogonal in physical space, see figure 2. In this figure a side view of the computational mesh is shown, where only every 10th mesh line is displayed. For conciseness we use a tensor notation with summation convention. Since only

https://doi.org/10.1017/S0022112006000930 Published online by Cambridge University Press

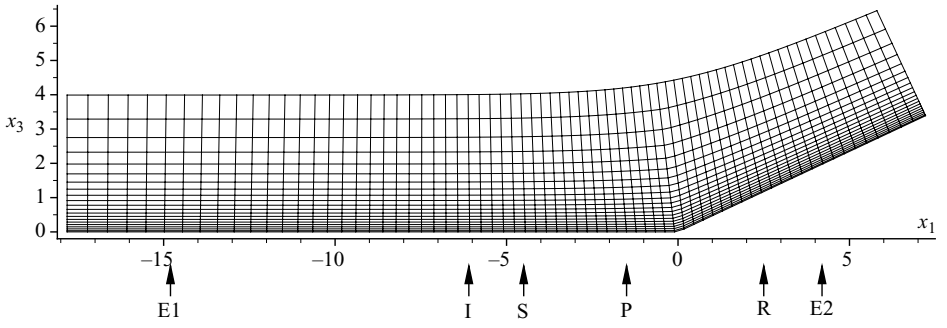


FIGURE 2. Computational mesh (each 10th line is shown); for selected reference stations as indicated by arrows refer to table 2 in § 4.

two-dimensional configurations in the (x_1, x_3)-plane are considered, the spanwise direction x_2 is orthogonal to the (x_1, x_3)-plane and ξ_2 is mapped onto x_2 linearly. Symbols refer to certain stations along the compression ramp which will be explained further in § 4.

The reference length throughout this paper is the mean boundary-layer thickness of the experiment, $\delta_0^* = 2.27\,\mathrm{mm}$, at the first reference section E1. The boundary-layer thickness is measured as the distance from the wall where 99 % of the mean free-stream velocity $U_\infty = 614.6\,\mathrm{ms}^{-1}$ is reached. Here and in the following, dimensional quantities are indicated by an asterisk. The integration domain has the extents $L_1 = 25.8$, $L_2 = 4$, $L_3 = 4$ at inflow. The computational mesh consists of $701 \times 132 \times 201$ points in the streamwise, spanwise, and wall-normal directions, respectively. We assume the solution to be L_2-periodic in x_2. The spatial resolution of the simulation is matched to that of Stolz *et al.* (2001*a*) in terms of wall units of the incoming boundary layer, which was found to be sufficient to reproduce DNS results with good accuracy. A perfect gas with a specific-heats ratio of $\gamma = 1.4$ is assumed and the viscosity is calculated according to Sutherland's law with a reference temperature $T_\infty^* = 108$ K. The non-dimensionalization is as follows:

$$u_i = u_i^*/U_\infty^*, \quad \rho = \rho^*/\rho_\infty^*, \quad T = T^*/T_\infty^*, \quad p = p^*/(\rho_\infty^* {U_\infty^*}^2), \quad E = E^*/(\rho_\infty^* {U_\infty^*}^2).$$

Here, u_i denotes the Cartesian velocity component in the x_i-direction, ρ is the density, p is the pressure and $E = p/(\gamma - 1) + \rho u_i u_i/2$ is the total energy. Reference data are taken from the experiment as $\rho_\infty^* = 0.314\,\mathrm{kg\,m}^{-3}$ and $T_\infty^* = 108\,\mathrm{K}$. The time t is non-dimensionalized by the characteristic time scale of the mean incoming boundary layer at the reference station E1, $\delta_0^*/U_\infty^* = 3.69\,\mu\mathrm{s}$.

The compressible Navier–Stokes equations in curvilinear coordinates are written as

$$\frac{\partial}{\partial t}\frac{f}{J} + \frac{\partial}{\partial \xi_1}\frac{F_E}{J} + \frac{\partial}{\partial \xi_2}\frac{G_E}{J} + \frac{\partial}{\partial \xi_3}\frac{H_E}{J} = \frac{\partial}{\partial \xi_1}\frac{F_S}{J} + \frac{\partial}{\partial \xi_2}\frac{G_S}{J} + \frac{\partial}{\partial \xi_3}\frac{H_S}{J}, \tag{2.1}$$

where the conservative variables are $f = \{\rho,\ \rho u_1,\ \rho u_2,\ \rho u_3,\ E\}$, and J is the Jacobian of the mapping $(x_1, x_2, x_3) \leftrightarrow (\xi_1, \xi_2, \xi_3)$. F_E, G_E, H_E are the convective fluxes and F_S, G_S, H_S are the diffusive fluxes in the respective coordinate directions. Further details can be found in Adams (1998).

For LES, equation (2.1) is filtered at the expense of the appearance of unclosed SGS terms. The resulting equations are solved with respect to the filtered variables $\bar{f} = G * f$, where G is the filter kernel and $*$ denotes a convolution operation. For closure, the approximate deconvolution model (ADM) of Stolz *et al.* (2001*a*) is used. A detailed description of ADM can be found in that reference and in Stolz,

https://doi.org/10.1017/S0022112006000930 Published online by Cambridge University Press

Adams & Kleiser (2001*b*). Here we only summarize the most important facts. With ADM a discrete filter G is explicitly applied along with its approximate inverse, the deconvolution operator $Q_N \approx G^{-1}$. The operator Q_N is applied to the filtered variables $\bar{f}$ in order to approximate the unfiltered variables by $f^\star = Q_N * \bar{f}$. A key feature of ADM is that the flux terms in (2.1) are computed directly using the approximately unfiltered fields $f \approx f^\star$ which are subsequently filtered explicitly with the discrete filter G. To model the transfer of energy to scales which cannot be represented on the computational mesh a relaxation term is added. No *a priori* estimates for model parameters are needed. Inverse relaxation times for density, momentum and energy are determined dynamically. The equations solved have the following form:

$$\frac{\partial}{\partial t}\frac{f}{J} + G * \frac{\partial}{\partial \xi_1}\frac{F_E}{J} + G * \frac{\partial}{\partial \xi_2}\frac{G_E}{J} + G * \frac{\partial}{\partial \xi_3}\frac{H_E}{J} = G * \frac{\partial}{\partial \xi_1}\frac{F_S}{J} + G * \frac{\partial}{\partial \xi_2}\frac{G_S}{J} + G * \frac{\partial}{\partial \xi_3}\frac{H_S}{J} - \chi(I - Q_N * G) * f, \quad (2.2)$$

where all fluxes are computed with the approximately deconvolved solution $f^* = Q_N * f$. The relaxation parameter χ is estimated dynamically Stolz *et al.* (2001*a*). For simplicity we will omit the overbar on filtered quantities in the following, implying that all variables are filtered variables if not mentioned otherwise.

For numerical integration, equation (2.2) is discretized on the mesh described above. A sixth-order compact finite-difference scheme of Lele (1992) is used for discretizing all spatial derivatives at the interior mesh points. A scheme of fourth-order accuracy is used at the first point off the domain boundary, and a one-sided scheme with third-order accuracy is used at the boundary. Time advancement is done with an explicit low-storage third-order Runge–Kutta scheme (Williamson 1980). The time-step size is determined dynamically by a CFL condition (CFL = 0.5). For the compression-corner computation the time-step size typically assumes values of about $1 \times 10^{-3}\delta_0/U_\infty$. It is well known that linear central finite-difference discretizations are generally not suitable for capturing shocks. However, Stolz *et al.* (2001*a*) have demonstrated that for finite Reynolds number ADM is able to reproduce the filtered-shock solution without local coupling to shock-capturing schemes. It should be emphasized that the exact filtered shock solution, where the high-wavenumber part of the spectrum has been removed, is slightly oscillatory owing to the Gibbs phenomenon. During the simulations it can occur that at isolated instances small flow regions are marginally resolved. In these cases, the deconvolution applied to the filtered temperature which is required for computing the energy transport term overamplifies numerical errors and can result in negative deconvolved temperatures. Note that ADM is designed to amplify non-resolved scales before the computation of the nonlinear transport. In such cases the deconvolved temperature is substituted by the filtered temperature in the neighbourhood of where the event occurred. This approach is known as Landweber projection in regularized-deconvolution procedures when *a priori* bounds on the deconvolved solution are possible (Bertero & Boccacci 1998). During our simulations these events occurred rarely (about once per 2000 time steps at a few random points near mean-flow separation) so that an adverse effect on the results can be excluded.

Boundary data are imposed as follows. At inflow we prescribe all variables f in time, using data from a separate boundary-layer computation, see § 3. Periodic boundary conditions were applied in the spanwise direction. At the outflow, a sponge-layer technique is used (Adams 1998). At the upper truncation plane of the computational domain non-reflecting conditions combined with a sponge layer are imposed. The

https://doi.org/10.1017/S0022112006000930 Published online by Cambridge University Press

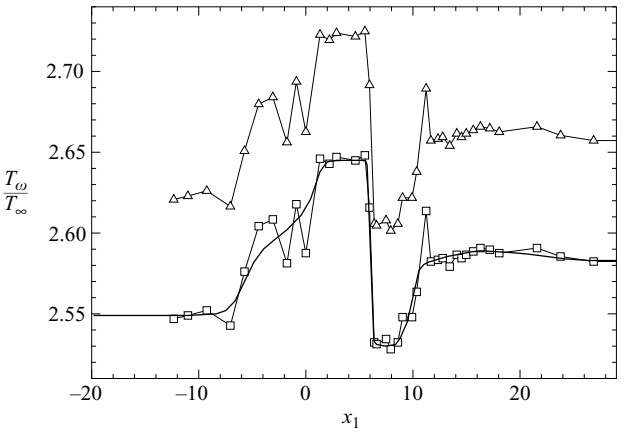


FIGURE 3. Streamwise distribution of the wall temperature: ——, smoothed and interpolated values; —△—, experimental data (Zheltovodov *et al.* 1990); —□—, rescaled to T_w of the reference experiment.

wall is assumed to be isothermal and no-slip conditions are enforced on the velocity. The wall-temperature distribution is uniform in the spanwise direction; along the streamwise direction it is taken from the experiment of Zheltovodov *et al.* (1990). The data from the experiment were rescaled by the wall temperature of the undisturbed boundary layer, smoothed and interpolated onto the computational grid, as shown in figure 3. Isothermal wall boundary conditions are preferable to adiabatic conditions since for the experiment an almost constant temperature distribution in time was observed during the measurements.

3. Flat-plate boundary-layer simulation results

A well-known problem in the simulation of turbulent boundary layers is that realistic inflow data are needed. We follow here the approach of Adams (2000) where a separate boundary-layer computation was performed from which a time series of data was sampled. This time series was made periodic in time and fed into the compression-ramp DNS. Also, the experimental boundary-layer parameters at reference station E1 need to be matched. This is accomplished by the rescaling and recycling technique of Lund, Wu & Squires (1998), formulated for compressible flow by Stolz & Adams (2003). Otherwise the numerical discretization and SGS model are the same as for the compression-ramp computation. For the flat plate the computational domain is rectangular with a streamwise extent of $L_1 = 16$ and the same extents in the spanwise and wall-normal directions as for the compression-corner case at inflow. The mesh consists of $201 \times 132 \times 101$ grid points. As initial data an instantaneous solution was taken from the previous flat-plate simulations of Stolz & Adams (2003) and rescaled to match the required Mach number and domain size.

Once a statistically stationary state had been reached after an initial transient, the simulation was continued for $55.4\delta_0/U_\infty$ characteristic time scales. For all conservative variables (density, momentum and total energy) 400 samples were taken at evenly spaced consecutive time increments roughly spaced by $0.14\delta_0/U_\infty$ at the downstream position $x_1 = 11$, where inflow transients of the flat-plate simulation have decayed. Subsequently, data were interpolated by sixth-order splines in the wall-normal direction to the finer grid which is used for the compression-corner simulation.

https://doi.org/10.1017/S0022112006000930 Published online by Cambridge University Press

	δ_0	δ_1	δ_2	Re_{δ_2}	$C_f \times 10^3$	H_{12}
Experiment	1	0.35	0.066	1826	1.79	5.3
Computation	1.04	0.38	0.074	2046	2.05	5.19
Difference	4 %	8.6 %	12.1 %	12.1 %	14.5 %	2 %

TABLE 1. Summary of mean-flow parameters for the flat-plate boundary layer simulation.

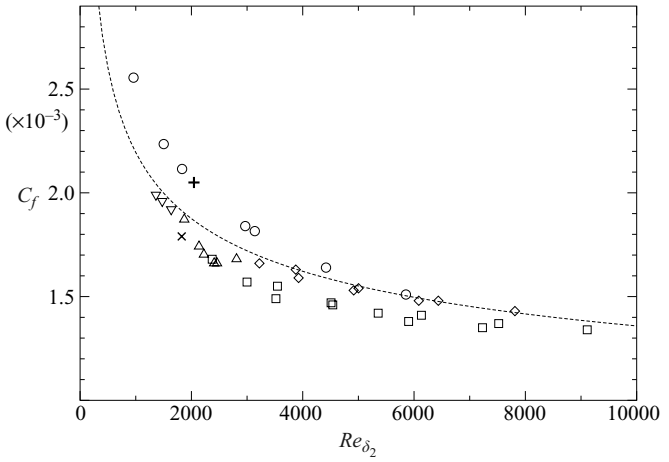


FIGURE 4. Skin-friction coefficient dependence on Reynolds number Re_{δ_2}: +, current LES; ×, reference experiment; □, Mabey *et al.* CAT7402 ($M_\infty = 3$); ◇, Mabey *et al.* CAT7402 ($M_\infty = 2.8$); △, Maier CAT7003 ($M_\infty = 2.9$); ○, Stalmach CAT5802 ($M_\infty = 2.75$); ▽, Laderman & Demetriades CAT7702 ($M_\infty = 3$) – – – –, prediction by von Kárman–Schönherr skin-friction law with van-Driest-II transformation. Data from Fernholz & Finley (1977, 1981).

To allow for a longer time advancement of the ramp computation than the sampling-time period of the inflow data these data are repeated periodically in time. The inflow-data sampling interval T_{samp} was chosen in such a way that a strong scale separation $T_{SSSM} \ll T_{samp} \ll T_{LSSM}$ between the characteristic time scales of sampling $T_{samp} = 55.4\delta_0/U_\infty$, small-scale shock motion $T_{SSSM} \sim O(\delta_0/U_\infty)$, and large-scale shock motion $T_{LSSM} \sim O(702\delta_0/U_\infty)$ was satisfied. This also could have been accomplished by requiring $T_{samp} \gg T_{LSSM}$. In this case, however, the inflow-data computation would have been computationally as expensive as the compression-ramp simulation itself.

Note that although the inflow data are statistically homogeneous in the spanwise direction and in time by construction, a small inhomogeneity can be found in the computed averages. For an interested reader the inflow data arrays are available from the authors upon request.

Mean-flow characteristics for the reference section E1 are summarized and compared with the experiment in table 1: δ_1 and δ_2 are displacement and momentum thickness, respectively; Re_{δ_2} is the Reynolds number based on free-stream velocity, momentum thickness and viscosity at the wall; H_{12} is the shape factor. The agreement of δ_0, δ_1, δ_2, H_{12} with the experiment is good. The computed skin-friction coefficient C_f differs more significantly from the experimental value. However, the discrepancy is within the limits of experimental-data scatter, as shown in figure 4. In this figure several experimental data sets C_f versus Re_{δ_2}, taken from Fernholz & Finley (1977, 1981), are shown along with our computed values and the experimental reference

https://doi.org/10.1017/S0022112006000930 Published online by Cambridge University Press

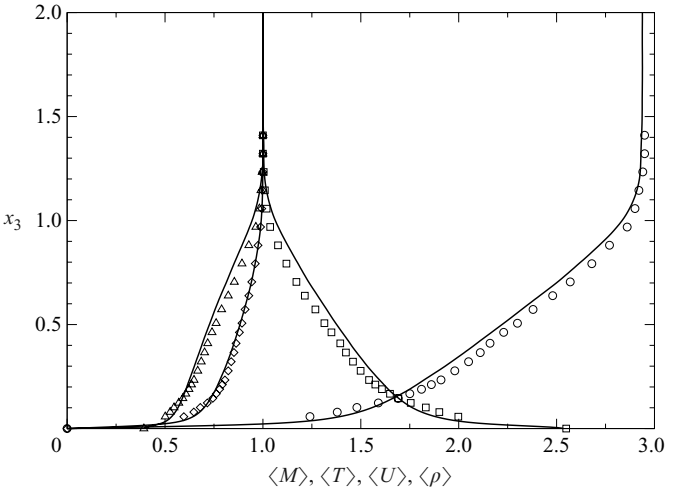


FIGURE 5. Wall-normal distributions of the mean flow for the incoming flow at station E1: ——, current LES; ○, Mach number; □, temperature; ◇, velocity; △, density. Symbols denote data from the reference experiment.

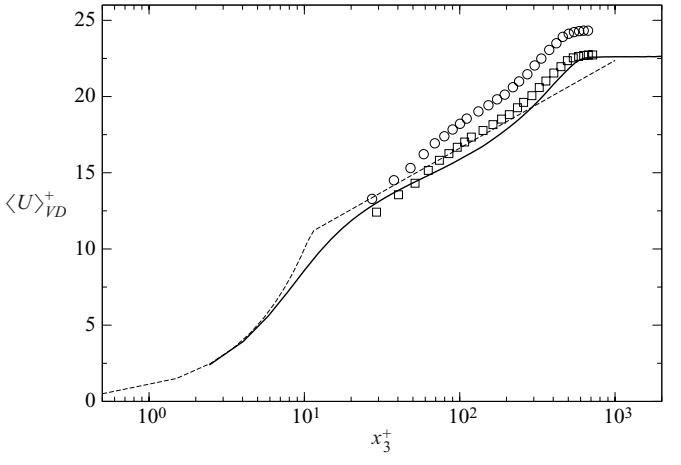


FIGURE 6. The van-Driest transformed mean-velocity profiles for the incoming flow at station E1. ○, reference experiment; ——, present LES; – – – –, linear and log-law $\ln x_3^+/0.4 + 5.1$; □, reference experiment with corrected C_f.

values at station E1. An empirical fit of the experimental data is shown by the dashed line, using a von Kárman–Schönherr incompressible skin-friction formula, extended to the compressible case by the van-Driest-II transformation (Hopkins & Inouye 1971). Note that the smaller the Reynolds number the larger the experimental-data scatter, indicating the increasing difficulty in obtaining a developed turbulent boundary layer.

The wall-normal distribution of mean Mach number, temperature, velocity, and density are compared with the experimental data in figure 5. In the bulk, the computed velocity profile agrees well with the experimental data, and minor discrepancies can be observed for the density and temperature profiles. These differences are well within the experimental error margin. The computed van-Driest-transformed velocity profiles, shown in figure 6, agree well with the logarithmic law of the wall

https://doi.org/10.1017/S0022112006000930 Published online by Cambridge University Press

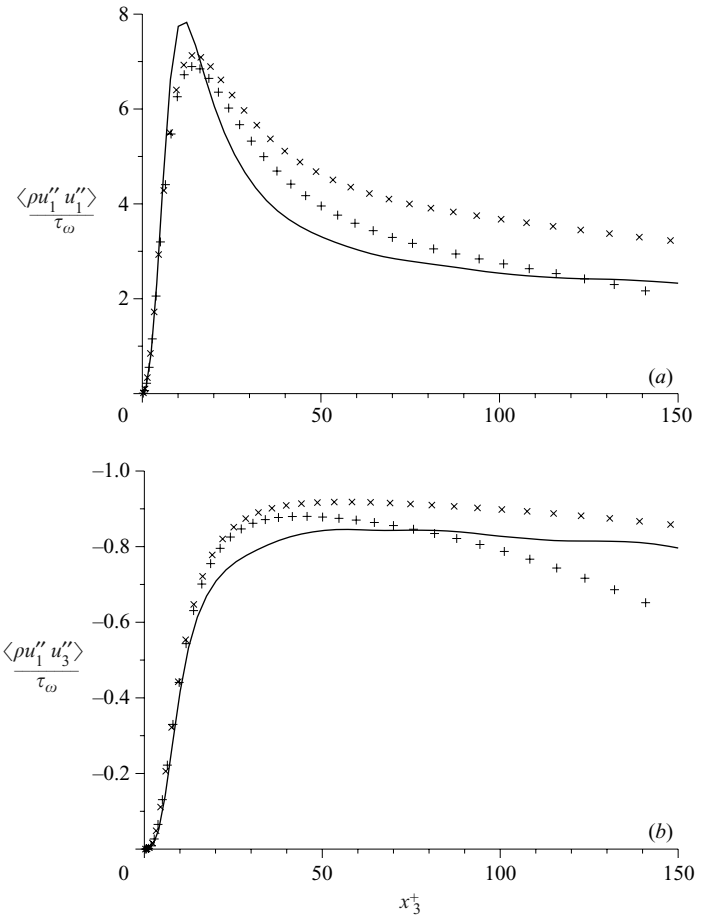


FIGURE 7. Profiles of (*a*) the density-weighted Reynolds-normal stress and (*b*) the density-weighted Reynolds-shear stress in wall units at station E1: ——, present LES; +, $Re_\theta = 670$; ×, $Re_\theta = 1410$. Symbols denote DNS data of Spalart (1988*b*).

$U_{VD}^+ = \ln x_3^+/0.4 + 5.1$. The velocity U_{VD} is computed as defined by Bradshaw (1977) and scaled by the wall-friction velocity $u_\tau = \sqrt{\tau_w/\rho_w}$. The wall-normal coordinate in wall units is $x_3^+ = u_\tau x_3/\nu_w$. In wall units the experimental data, shown as open circles, differ more significantly from the law of the wall. A better agreement with the law of the wall is obtained if the experimental U_{VD} is scaled with u_τ of the simulation (open squares).

With respect to inner variables the density-weighted Reynolds-normal-stress and Reynolds-shear-stress profiles should agree with incompressible data in the near-wall region (Smits & Dussauge 1996). This is the case for our simulation data in the region $x_3^+ < 20$ as shown in figure 7 by a comparison with incompressible DNS of Spalart (1988*a*).

4. Compression-corner flow

For the analysis of the compression-corner flow we will refer to selected downstream stations as indicated in figure 2. The positions of these stations in terms of the

https://doi.org/10.1017/S0022112006000930 Published online by Cambridge University Press

Symbol	x_1	Comment
E1	−15.4	experimental reference section 1
I	−6.1	incipient interaction
S	−4.5	mean-flow separation
P	−1.5	pressure plateau position
R	2.5	mean-flow reattachment
E2	4.4	experimental reference section 2

TABLE 2. Selected downstream stations.

Parameter	Value	Comment
β	25°	
M_∞	2.95	
Re_{δ_0}	63560	
Re_{δ_1}	22120	
Re_θ	4705	using ν_∞
Re_{δ_2}	2045	using ν_w
δ_1	0.37	at section E1
θ	0.071	at section E1
N_1	701	
N_2	132	
N_3	201	
L_1	25.8	along the wall
L_2	4	
L_3	≈ 4	
$\Delta^+_{x_1}$	16 to 34	
$\Delta^+_{x_2}$	17.8	at section E1
$\Delta^+_{x_3}$	1.1	first point off the wall at section E1

TABLE 3. Simulation parameters.

downstream coordinate x_1, along with their particular significance, are summarized in table 2. An overview of all relevant flow parameters is given in table 3. Additionally, the number of grid points N_i is specified for each coordinate direction $i = 1, 2, 3$. The extent of the computational domain in the streamwise direction is L_1, in the spanwise direction L_2, and in the wall-normal direction at inflow L_3. Measured in wall units of the incoming boundary layer the grid size in the respective coordinate directions is given as $\Delta^+_{x_i}$, where for the wall-normal direction this refers to the distance of the first grid point off the wall.

The ramp computation was started from synthetic initial data generated by an inviscid flow field superimposed with a laminar flat-plate boundary layer. After an initial transient the compression-corner simulation was continued for 703.45 characteristic time scales of the incoming boundary layer δ_0/U_∞. This corresponds to about 27 flow-through times of the free stream through the computational domain and is about twice as long as for the earlier DNS of Adams (2000). Owing to the larger sampling time, smoother statistical data have been obtained, and also at least one period of low-frequency large-scale shock motion (LSSM) could be captured (see § 4.2). During this time interval the flow field was sampled 1272 times for statistical analysis. Various statistical quantities and time-history data have been saved. This calculation required about 18000 CPU hours on 4–6 CPU running in parallel on vector-parallel platforms NEC SX-5 and SX-6.

https://doi.org/10.1017/S0022112006000930 Published online by Cambridge University Press

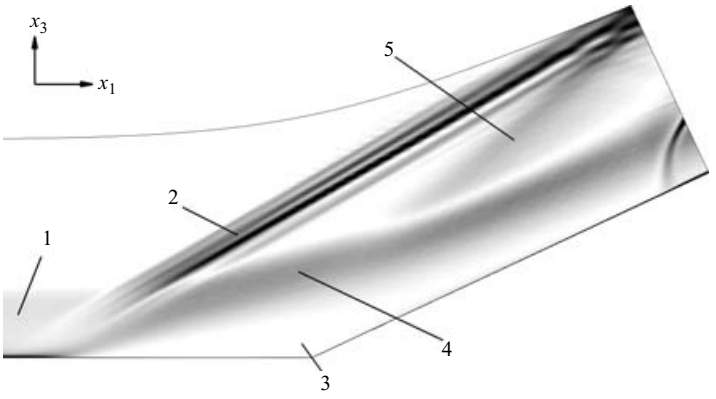


FIGURE 8. Mean density gradient $\|\nabla\rho\|$ averaged in spanwise direction (for legend see text).

In the following we present data along certain computational-grid lines $\xi_1 = \text{const}$, as indicated in figure 2. The relevant positions are marked with letters which we refer to in the following. The velocity is represented by its contravariant components, $u_1^c = (u_1\partial\xi_1/\partial x_1 + u_3\partial\xi_1/\partial x_3)/\sqrt{(\partial\xi_1/\partial x_1)^2 + (\partial\xi_1/\partial x_3)^2}$, $u_2^c = u_2$, and $u_3^c = (u_1\partial\xi_3/\partial x_1 + u_3\partial\xi_3/\partial x_3)/\sqrt{(\partial\xi_3/\partial x_1)^2 + (\partial\xi_3/\partial x_3)^2}$. The computational grid is constructed in such a way that the difference between contravariant components and longitudinal components, where the velocity is rotated into a Cartesian system aligned with the wall, is small. The contravariant projection, however, removes the ambiguity of the longitudinal projection near the corner. We distinguish between Favre, i.e. density-weighted, statistical averages and Reynolds averages. The former is indicated by a double prime $f'' = f - \langle\rho f\rangle/\langle\rho\rangle$, the latter by a single prime $f' = f - \langle f\rangle$.

4.1. *Mean flow*

For a general impression of the flow a Schlieren-imitation (density-gradient magnitude) of the mean flow in the interaction region is shown in figure 8. A corresponding Schlieren photograph of the reference experiment would require an exposure of about 2.6 ms. Note that the flow near the outflow boundary is affected by the sponge outflow treatment where artifacts can be seen, which are, however, not relevant for our analysis. The computed flow recovers the main flow features that were described in § 1. The ramp deflection angle of $\beta = 25^\circ$ at $M_\infty = 2.95$ is large enough for the incoming boundary layer (1 on figure 8) to separate. Where the large near-wall density gradient of the incoming boundary layer detaches from the wall the separation region (3) begins. A detached shear layer (4) contains the reverse flow region (3). Since the Reynolds number is comparatively large, the forward shock (2) penetrates rather deeply into the boundary layer. Near the wall increased turbulent diffusion and finite mean streamline curvature cause the shock foot to spread out so that it is hardly visible in the Schlieren image. LSSM and spanwise shock deformation give rise to apparent additional shock images around the main compression shock. The rear compression shock (5) appears as a converging set of compression waves originating from the reattachment region. Instantaneous data will show, however, that the rearward shock is in fact created by highly unsteady compression waves and shocklets.

Another important finding can be obtained from figure 9. The computational-domain boundaries are indicated by thin black lines; crossflow-planes are coloured with respect to local mean temperature. A translucent isosurface of mean pressure $\langle p\rangle = 0.1$ represents the mean forward shock. Despite the fact that the flow geometry

https://doi.org/10.1017/S0022112006000930 Published online by Cambridge University Press

https://doi.org/10.1017/S0022112006000930 Published online by Cambridge University Press

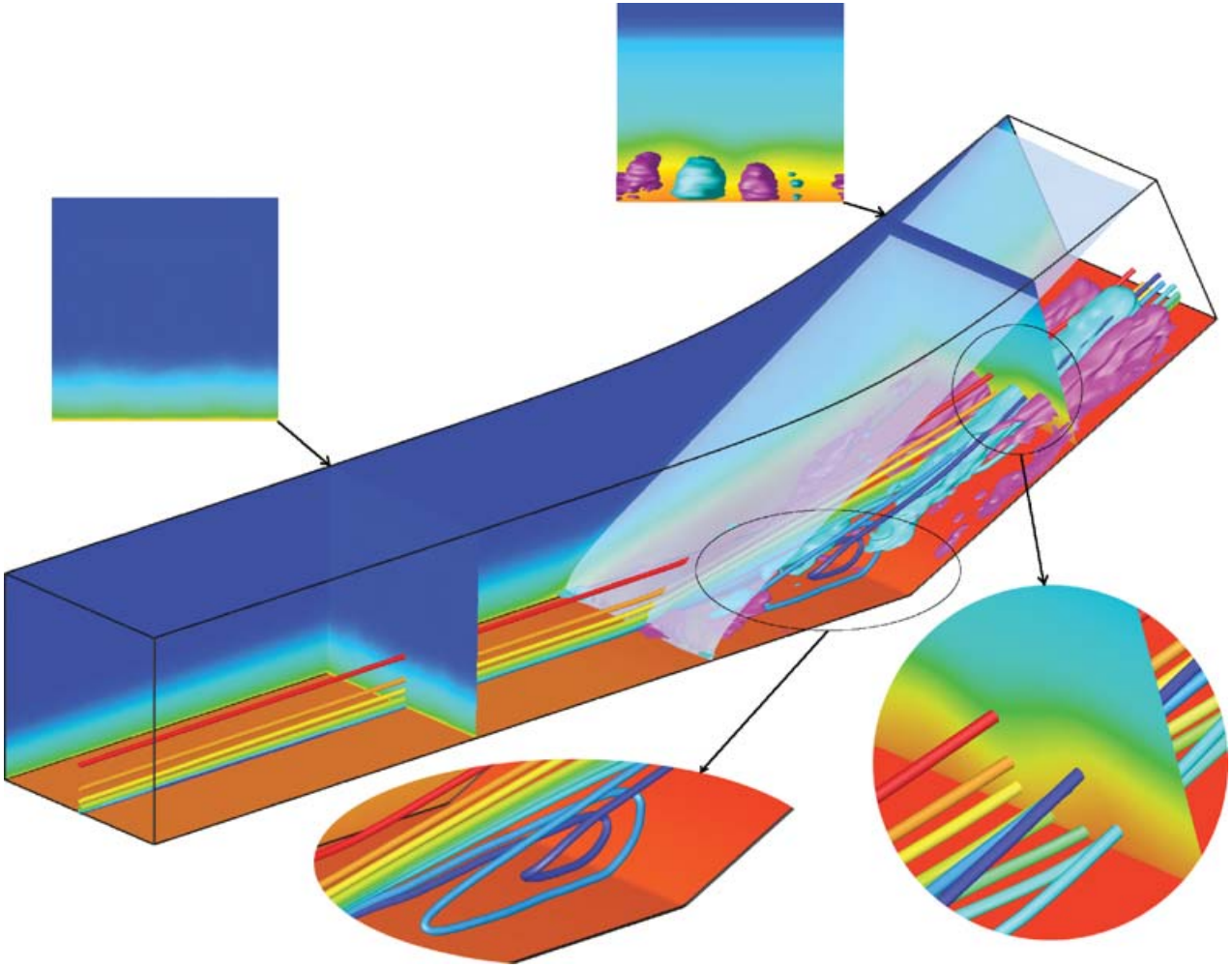


FIGURE 9. Three-dimensional mean flow. Colours denote temperature.

is nominally two-dimensional, the interaction breaks the spanwise translational symmetry. The temperature distribution in a cross-flow plane after the interaction clearly shows a spanwise variation, unlike a cross-flow plane before the interaction. A rake of 10 coloured mean streamlines identifies the recirculating flow in the separation region. Furthermore, a non-planar motion in the separation zone and a rotational motion after reattachment are evident.

Two pairs of counter-rotating streamwise vortices can be identified in the reattaching shear layer from isosurfaces of contravariant streamwise vorticity. Since the circulation of these vortices is rather small which makes them hard to extract from background noise, the streamwise mean vorticity was additionally filtered by a top-hat filter on the computational mesh for the purpose of visualization. Positive rotation is indicated by the colour 'cyan' and negative rotation by 'magenta'.

These streamwise vortices affect turbulence structure and the properties of the mean flow significantly (Inger 1977; Brazhko 1979; Zheltovodov *et al.* 1983; Zheltovodov & Yakovlev 1986; Floryan 1991; Lüdeke *et al.* 2004). This is evident if we consider the computational analogue of an experimental oil-flow image in figure 10, where we show the distribution of the mean skin-friction coefficient. Solid lines represent the contour $C_f = 0$, the left-most line representing separation, the right-most reattachment; the darker colour corresponds to the lower value of the the skin friction. For reference, the corner is indicated by a dashed line. It is evident that although the separation line is more or less two-dimensional without significant variations in the spanwise direction, the reattachment line clearly exhibits two pairs of flow convergence and divergence lines. The position of the convergence lines is approximately $x_2 \approx \delta_0$ and $x_2 \approx 3\delta_0$, and the position of the divergence lines approximately $x_2 \approx 2\delta_0$ and $x_2 \approx 4\delta_0$. The convergence lines can be attributed to cross-flow uplift and the divergence lines to cross-flow downwash, so that they represent footprints of two-pairs of counter-rotating streamwise vortices. Consistently with experimental observations (e.g. Floryan 1991) we find that the spanwise width of each vortex pair is about $2\delta_0$. A surface oil-flow visualization obtained in the experiments of Zheltovodov *et al.* (1983) and Zheltovodov & Yakovlev (1986) exhibits similar features; for the higher-Reynolds-number experiment a photo of oil-flow vizualization is shown in figure 11. The characteristic pattern can be associated with a system of steady streamwise vortices. Again the vertical dashed line indicates the position of the ramp corner. The accumulation of oil downstream shows the typical mean-flow reattachment topology in the presence of streamwise vortices (Zheltovodov *et al.* 1983; Lüdeke *et al.* 2004). Clearly visible are convergence and divergence lines in the reattaching flow, also penetrating upstream into the separation zone, pairs of convergence and divergence lines being spaced by approximately $2\delta_0$. It should be noted that the computational domain size of $4\delta_0$ with periodic boundary conditions applied in spanwise direction allows flow structures with spanwise periodicity of at most $4\delta_0$ to be captured. We therefore cannot exclude the existence of vortical structures with larger spanwise periodicity. Such structures, however, have not been observed experimentally.

The question arises about the origin of these streamwise vortices. A stability analysis of the turbulent mean flow is beyond the scope of this paper, even if the question of whether such a kind of analysis is valid for turbulent flows is put aside. Görtler vortices arise from an instability of a laminar boundary layer with sufficiently concave streamwise curvature. If the mean streamline curvature in the separation region or in the reattachment region is larger than the critical value for laminar flow a similar mechanism for generating streamwise vortices may be active in the turbulent flow as

https://doi.org/10.1017/S0022112006000930 Published online by Cambridge University Press

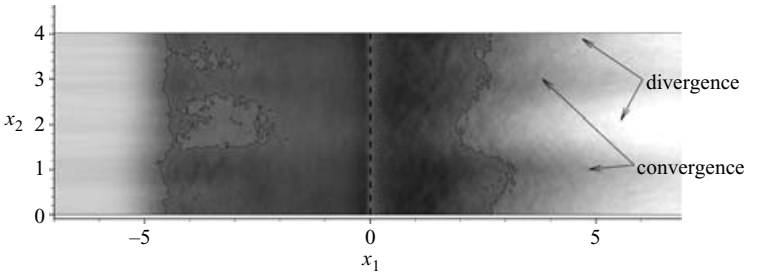


FIGURE 10. Distribution of the mean skin-friction coefficient: ——, $C_f = 0$; - - - -, corner position.

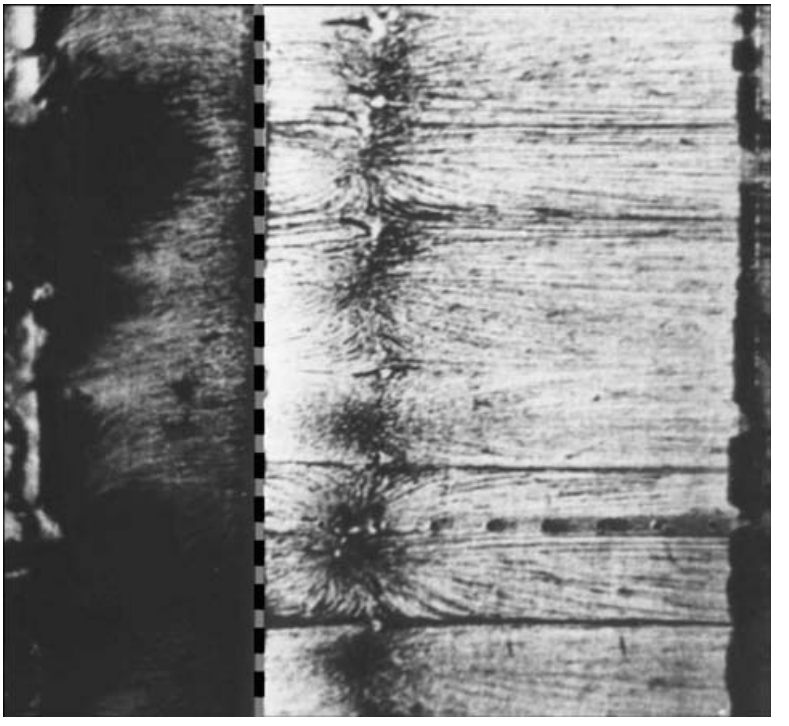


FIGURE 11. Oil-flow visualization pattern from higher-Reynolds-number experiment; the thick dashed vertical line indicates the corner position.

well. The Görtler number for a turbulent boundary layer can be estimated as

$$G_T = \frac{\theta}{0.018\delta_1}\sqrt{\frac{\theta}{R}}$$

(Smits & Dussauge 1996, p. 277), where R is the curvature radius of the mean-flow streamlines within the boundary layer close to the corner, θ is the momentum thickness and δ_1 the displacement thickness. Near the separation region all streamlines within the boundary layer have $G_T > 1$ which is well above the critical value of about 0.6 for laminar flows (Görtler 1954). G_T is slightly smaller in the reattachment region but still near the critical value. Another criterion for the significance of streamline curvature is given by the curvature parameter δ_0/R which was used for the investigation of subsonic turbulent flows (Floryan 1991). From our simulation we find $\delta_0/R > 0.1$

https://doi.org/10.1017/S0022112006000930 Published online by Cambridge University Press

near the separation line and $\delta_0/R \geqslant 0.03$ near reattachment. Again these values are much larger than the critical value $\delta/R = 0.01$, for which Floryan (1991) found the first appearance of streamwise vortices. These two indicators, Görtler number and curvature parameter, point to a Görtler-like mechanism being responsible for the observed streamwise vortices.

For a statistically two-dimensional turbulent flow there is no reason why the observed streamwise vortices should remain steady at a fixed spanwise position. Steady or very low-frequency spanwise variations within the incoming boundary layer or model imperfections can result in fixing the spanwise location of the vortices, as was observed by Lüdeke *et al.* (2004) and pointed out by Floryan (1991). Owing to limited statistical sampling the incoming boundary layer is not perfectly two-dimensional in the means. It contains steady disturbances over a range of spanwise wavenumbers with an amplitude of at most $0.03U_\infty$. It was found that there is no dominant spanwise wavelength at the inflow (the spectral distribution is broadband), and no correlation with reattachment region was observed. These steady disturbances can act as a seed similarly to experimental-model imperfections and probably determine the Görtler-like vortex locations. It should be emphasized that the spanwise wavenumber of the Görtler-like vortices (and thus their size) is determined by their generating mechanism and not by the seed.

The spanwise variation of the mean skin-friction coefficient at the reference stations E1, I, S, P, R, and E2 is shown in figure 12. Whereas C_f varies at station E1 in the undisturbed boundary layer by a magnitude of approximately $\pm 0.24 \times 10^{-3}$, this variation increases to about $\pm 0.69 \times 10^{-3}$ at station E2 after reattachment. It is obvious that the spanwise variation of the mean flow should be taken into account when comparing computational data with the experiment since experimental data usually are collected only at a single section $x_2 = \text{const}$ (usually the model centreline).

To assess the agreement of our computation with the experiment we compare skin-friction coefficient and surface pressure in figure 13. The mean skin-friction measurements were performed by the global interferometry skin friction technique (GISF) which has an estimated accuracy estimated of 6–10 % (Borisov *et al.* 1993, 1999). Several partially overlapping datasets were generated near the model centreline between convergence–divergence-line pairs, but the exact position, with respect to these is unknown. The computational data averaged in time and in the spanwise direction (thick solid line) are in very good agreement with the experimental data (circles), figure 13(*a*). Deviations of experimental data from computed spanwise-averaged values are between $\min_{x_2} C_f$ and $\max_{x_2} C_f$ denoted by dotted lines. We recall that in the computation the decompression corner is not considered. Instead, the deflected part of the compression ramp is longer than for the reference experiment and a sponge zone is added at the outflow of the computational domain. Therefore, no agreement of computational and experimental data can be expected near the decompression corner and beyond. The mean-flow separation is located at $x_{1S} = -4.5 \pm 0.25\delta_0$ and mean-flow reattachment occurs at $x_{1R} = 2.5 \pm 0.7\delta_0$. The separation length L_{sep} can be estimated as $7\delta_0$.

A less strong spanwise variation is observed for the surface pressure, shown in figure 13(*b*) normalized by the surface pressure of the incoming boundary layer at reference station E1. The surface pressure exhibits a plateau with an inflection point P as indicated in the figure. Again, a very good agreement between computational and experimental results is found. Here, we can also verify that differences between computation and experiment near the decompression corner are due to the mentioned differences in the length of the deflected part of the ramp and to the sponge zone.

https://doi.org/10.1017/S0022112006000930 Published online by Cambridge University Press

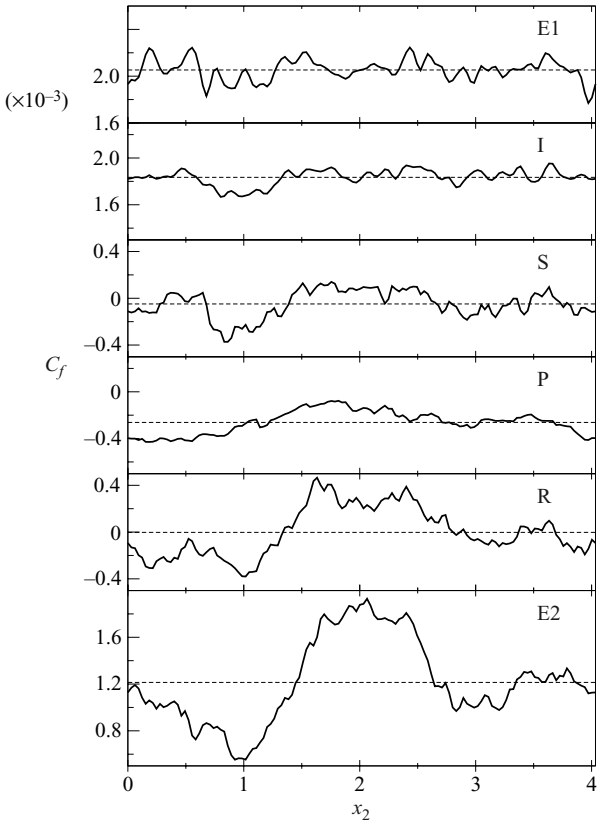


FIGURE 12. Distribution of the mean skin-friction coefficient at the wall in the spanwise direction: ——, averaged in time; – – – –, averaged in time and over the spanwise direction.

With open squares we also show in figure 13(*b*) surface-pressure data from the higher-Reynolds-number experiment with a longer deflected surface. First, we note that in the range considered the Reynolds number has a negligible effect on the surface pressure. Second, it can be seen that the computational data indeed follow the additional experimental data before they are affected by the outflow sponge zone. From comparison with experimental data the sponge zone invalidates a layer with a length of about δ_0 upstream of outflow.

For an analytic prediction of the separation location in shock–boundary-layer interaction, the free-interaction theory for large Reynolds numbers is frequently invoked (Chapman, Kuehn & Larson 1957). A result of this theory is an empirical formula for the surface pressure across the interaction region (Erdos & Pallone 1962)

$$F(s) = (p(s) - p_I)\sqrt{\frac{\sqrt{M_\infty^2 - 1}}{2C_{fI}}},$$

where $p(s)$ and p_I are the wall pressure normalized by the dynamic pressure $q = \frac{1}{2}\rho_\infty U_\infty^2$, as a function of the normalized streamwise coordinate

$$s = \frac{x - x_I}{x_S - x_I}.$$

https://doi.org/10.1017/S0022112006000930 Published online by Cambridge University Press

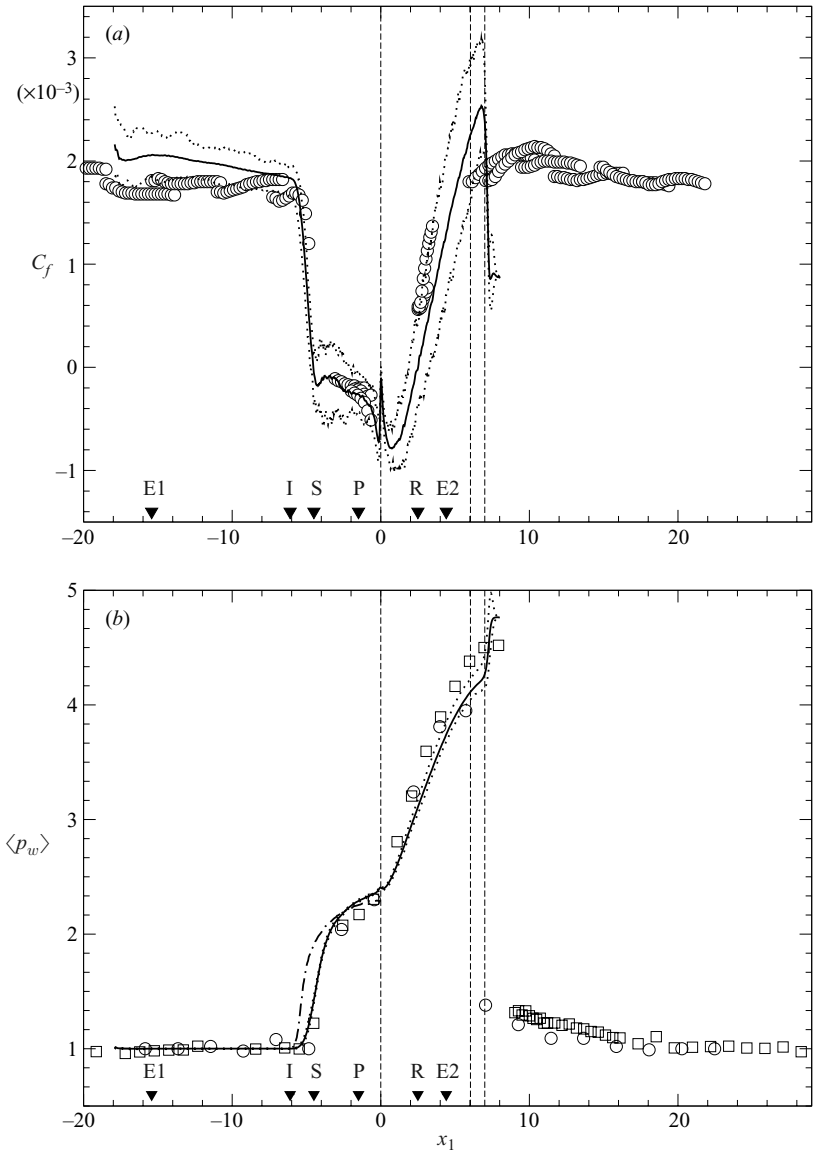


FIGURE 13. Averaged (*a*) skin-friction coefficient and (*b*) wall-pressure distributions in the streamwise direction: ○, reference experiment; ——, present LES averaged in time and over the spanwise direction; ·····, present LES averaged in time, min and max values over the spanwise direction; □, higher-Reynolds-number experiment; —·—, free interaction theory. The left-most dashed vertical line indicates the compression-corner position, the middle dashed vertical line the decompression corner of the experiment and the right-most dashed vertical line the beginning of the sponge-zone at the outflow of the computational domain. Although beyond the scope of the current paper, experimental data downstream of the expansion corner are provided for illustration.

The index *I* indicates that data are to be taken from the incoming undisturbed boundary layer just before the interaction. Although the free interaction theory predicts a steeper pressure rise and an earlier separation than is observed for experiment and LES, the predicted pressure-plateau value agrees with both.

https://doi.org/10.1017/S0022112006000930 Published online by Cambridge University Press

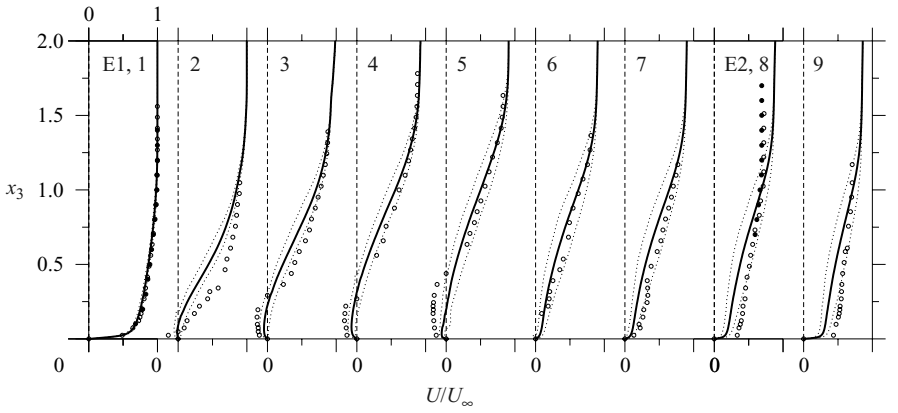


FIGURE 14. Velocity profiles at several downstream positions.

Section	x_1
1	−8.05
2	−2.93
3	−1.95
4	−1.22
5	1.22
6	2.68
7	3.05
8	4.15
9	5.73

TABLE 4. Additional streamwise stations.

Figure 14 gives an impression of the mean flow evolution. The computational data are shown by thick solid and dotted lines, having the same meaning as in figure 13. The black dots correspond to sections E1 and E2 of the reference experiment, and open circles indicate higher-Reynolds-number experimental data at sections 1–9; their streamwise positions are detailed in table 4. The incoming undisturbed turbulent boundary-layer profile in section 1 transforms into a profile with weak reverse flow slightly downstream of the separation point (section 2). Further downstream the reverse flow becomes stronger (sections 3–5). At section 6 the boundary layer is reattached while still showing a momentum deficit in the wake. This re-established attached boundary layer develops towards an undisturbed profile further downstream. The experimental profiles exhibit only a weak dependence on the Reynolds number in the range considered (only at sections 1 and 8 are data from both experiments available). Taking into account the spanwise variation of the computed mean velocity, experimental and numerical data generally agree well. Excessive negative experimental velocity data at section 5 can be explained by difficulties in measuring the reverse flow; also, near the line of the zero velocity accuracy and reliability of experimental data are reduced. Differences inside the boundary layer at section 2 ($x_3 < \delta_0$) and in the outer flow at section 8 ($x_3 > \delta_0$) may be attributed to difficulties with Pitot probes in the highly unsteady regions as pointed out by Dolling (1998). A Pitot probe overestimates data in these regions. Also, the accuracy of the static pressure

https://doi.org/10.1017/S0022112006000930 Published online by Cambridge University Press

measurements is very limited near unsteady shock waves and near separation and reattachment regions.

4.2. *Shock wave structure*

An impression of the instantaneous shock-wave structure can be obtained from a computed Schlieren-type visualization in figure 15. This is similar to figure 8; the flow snapshot is taken at a time instant, however, and corresponds roughly to an experimental spark shadowgraph. The numbers 1–5 refer to the same events as shown in figure 8. The spanwise variation of the shock position causes some smearing of the shock position in the interaction region after averaging in the spanwise direction. Clearly visible are compression waves (5) above the separated shear layer (4) and the rearward stem of the λ-shock which originates from the reattachment region. Also, the general shape of the forward shock appears to have changed slightly. A similar observation can be made for experimental visualizations at two different time instants for the higher-Reynolds-number experiment (Zheltovodov *et al.* 1983), shown in figures 15(c) and 15(d). An animation of a time-series of shock visualizations for our computation is available as a supplement to the online version of the paper which clearly shows the unsteady motion of the shock system and the shedding of compression waves behind the forward shock. We find in our simulations small-scale shock motion, as reported by Andreopoulos & Muck (1987) and Adams (2000), along with LSSM, as reported by Dolling & Murphy (1983). We also observe that the rearward shock is highly unsteady and becomes invisible at irregular time intervals. The compression waves, indicated as 5 in figure 15, travel downstream with a speed of about $0.1U_\infty$ to $0.4U_\infty$.

It is found that waves travelling at the larger speed are shocklets. Their speed is of the same order of magnitude as the convection velocity of the largest eddies in the detached shear layer (4) so that the ambient-flow speed is supersonic relative to these eddies. For verification of the shocklet character of the stronger compression waves, we have confirmed that the change of the flow state across the shocklets satisfies the Rankine-Hugoniot conditions (Lee, Lele & Moin 1991) relative to the ambient flow behind the separation shock. The shocklet Mach number, defined as the ratio of ambient-flow velocity with respect to the shocklet and sound speed, varies between 1.23 and 2.2. The stronger shocklets with larger Mach number have lower absolute velocity and belong to the unsteady second stem of the λ-shock.

We believe that the presence of travelling compression waves and shocklets in the wake of the compression shock explains the high level of turbulent fluctuations in the external flow between the separation shock and the detached shear layer which was shown earlier in experiments by hot-wire measurements (Zheltovodov & Yakovlev 1986). The observed phenomenon provides evidence for an additional mechanism which enhances the level of turbulent fluctuations in this flow region along with direct interaction of shocks and turbulence (Andreopoulos *et al.* 2000; Anyiwo & Bushnell 1982). By the method of diagrams of Kovasznay (1953) it was shown by Zheltovodov & Yakovlev (1986) that the acoustic mode is prevalent in this region, which is consistent with the existence of weak shocklets.

For an analysis of shock motion Dolling & Or (1985) recorded the time evolution of wall-pressure signals to identify the shock-foot location. A direct comparison is possible if we apply a similar analysis to our computational data. Time-histories of wall pressure normalized by the mean value at station I are shown in figure 16 at six different downstream positions. Sensors were placed at the centreline of the domain,

https://doi.org/10.1017/S0022112006000930 Published online by Cambridge University Press

https://doi.org/10.1017/S0022112006000930 Published online by Cambridge University Press

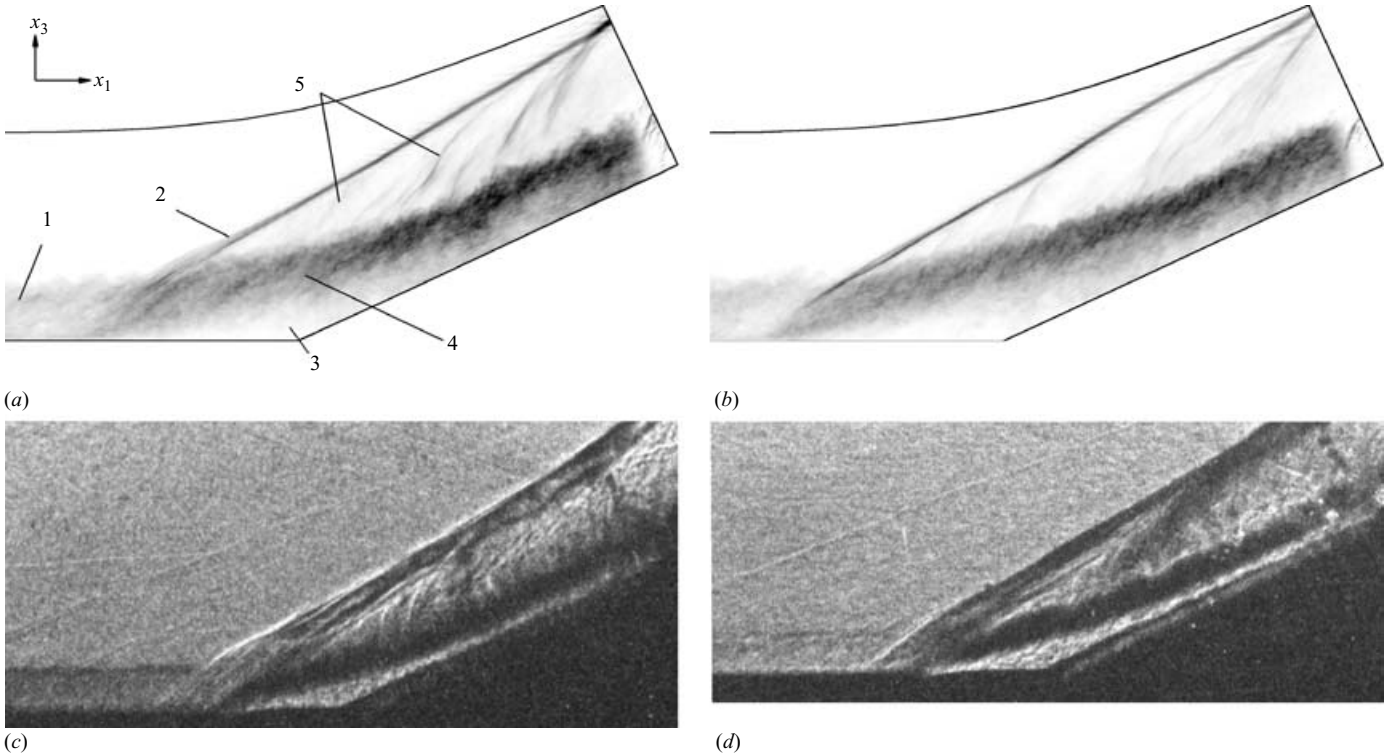


FIGURE 15. Schlieren-type vizualisation at two time instants: (a, b) simulation, computed as density gradient $\|\nabla\rho\|$ averaged in the spanwise direction; (c, d) higher Reynolds number experiment. Computational and experimental time instants are not related to each other. For a description of points 1–5 see figure 8.

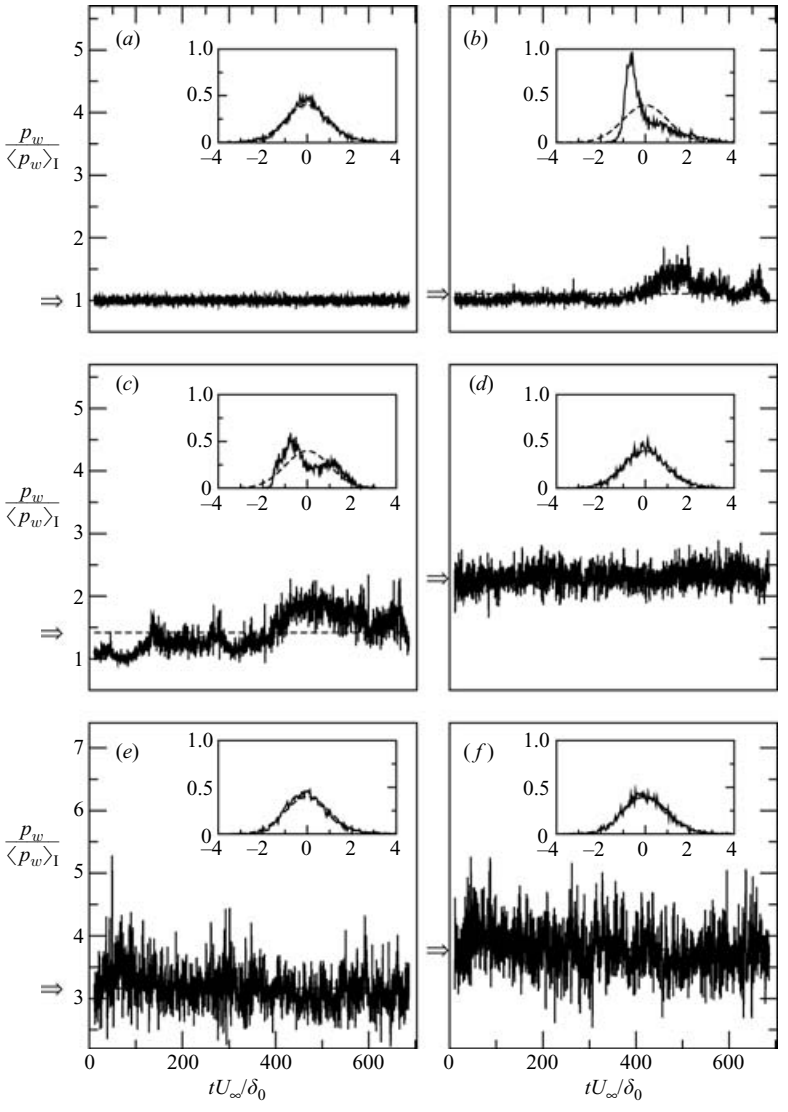


FIGURE 16. Wall pressure history and probability distributions at six different wall positions, (*a*) at I within the incoming boundary layer, (*b*) near the beginning of the interaction region, (*c*) near the location of maximum pressure fluctuations (refer to figure 17), (*d*) at P inside the separation region, (*e*) at R near reattachment, (*f*) at E2 downstream of reattachment. The time increment for the time-sequence sampling is about $0.1\delta_0/U_\infty$.

their streamwise positions corresponding to:

(*a*) within the undisturbed boundary layer at station I,

(*b*) near the beginning of the interaction where mean pressure starts to rise above the value in the incoming boundary layer $\langle p \rangle = 1.1\langle p \rangle_I$ (see also figure 13*b*),

(*c*) maximum pressure fluctuation position (refer to figure 17),

(*d*) inside the separation region at station P (refer to figure 13),

(*e*) near the reattachment line at station R,

(*f*) downstream of the separation at the experimental station E2.

The arrows and thick dashed lines indicate the respective time-averaged pressure values. The insets in each figure show the normalized probability-density function

https://doi.org/10.1017/S0022112006000930 Published online by Cambridge University Press

(PDF) for the respective pressure signal. For reference a Gaussian PDF is also indicated by a dashed curve. Evidently the PDF distribution is essentially Gaussian within the incoming boundary layer, figure 16(*a*), and within the separation region, figure 16(*d*). The motion of the forward shock front manifests itself in the pressure fluctuations by the appearance of a PDF peak at negative pressure values near the onset of the interaction. The PDF also shows that the forward shock intermittently crosses the sensor position, pre-shock pressure values being more likely to be found than post-shock values. This finding agrees with the observations of Dolling & Or (1985). The streamwise length of the forward-shock excursion can be estimated as $1.3\delta_0$. Further evidence of LSSM can be found at the next sensor position, figure 16(*c*). Initially, the observed pressure is below its average value (the shock wave is downstream of the sensor position). Subsequently, the shock moves upstream, and pressure the increases beyond its average value at about $400\delta_0/U_\infty$. At the end of the observation time interval the pressure roughly recovers its initial value. Given a limited observation time interval a LSSM time scale cannot be deduced quantitatively. For this purpose, the simulation should cover several cycles of shock motion. Since such a requirement would multiply computational cost by at least a factor of two this is impractical for us.

We find a PDF with a single off-centre peak at the beginning of the interaction and a double-peaked PDF within the interaction region. This reflects the highly intermittent shock motion which has been observed in earlier experiments (Dolling & Murphy 1983; Dolling & Or 1985).

Inside the separation zone, figure 16(*d*) and further downstream, figure 16(*e*), the PDF distributions resume a Gaussian shape. The qualitiative difference between the pressure signal in the intermittent region near the beginning of the interaction, figure 16(*b*), which is dominated by the separation shock motion, and the one near reattachment, figure 16(*e*), which is affected by the unsteady rearward stem of the λ-shock, suggests that the motion of the rearward stem is not related to the motion of the forward stem. Whereas several studies (e.g. Andreopoulos & Muck 1987; Adams 2000) indicate that the small-scale shock motion is driven by turbulent bursting events in the incoming boundary layer, there is currently no theory available which explains LSSM (Dolling 1998, 2001). It should be mentioned that in our simulation we can exclude that LSSM was driven by the periodically repeated inflow data since the time scales of LSSM and data repetition differ by about one order of magnitude.

Dolling & Murphy (1983) found a characteristic shape of the standard-deviation distribution of wall-pressure fluctuations across the interaction, figure 17(*a*). Normalized by the local mean wall pressure our computational results agree quantitatively with the experimental results of Dolling & Murphy (1983), although for these results the Reynolds numbers are one to two orders of magnitude larger. Since no Reynolds-number-independent scaling of the interaction-region extent is known, $\sigma(p_w)$ at locations corresponding to respective interaction events, such as separation location S, pressure-plateau location P and reattachment location R need to be compared. A global maximum at more than 20 % of the local mean wall pressure is observed for the LES in the separation region at $x_1 \approx -4.5\delta_0$ which corresponds to the mean separation position S, figure 17(*b*). The maximum value agrees well with the experimental data of Dolling & Murphy (1983) at larger Reynolds number. Note that Dolling & Murphy (1983) find the peak location to be slightly upstream of their measured separation point. The reason may be that the separation location was identified visually from a kerosene-lampblack streak pattern, whereas for the computation $C_f = 0$ could be identified directly. As discussed before, the observed large variance of pressure fluctuations is a consequence of the shock-foot motion.

https://doi.org/10.1017/S0022112006000930 Published online by Cambridge University Press

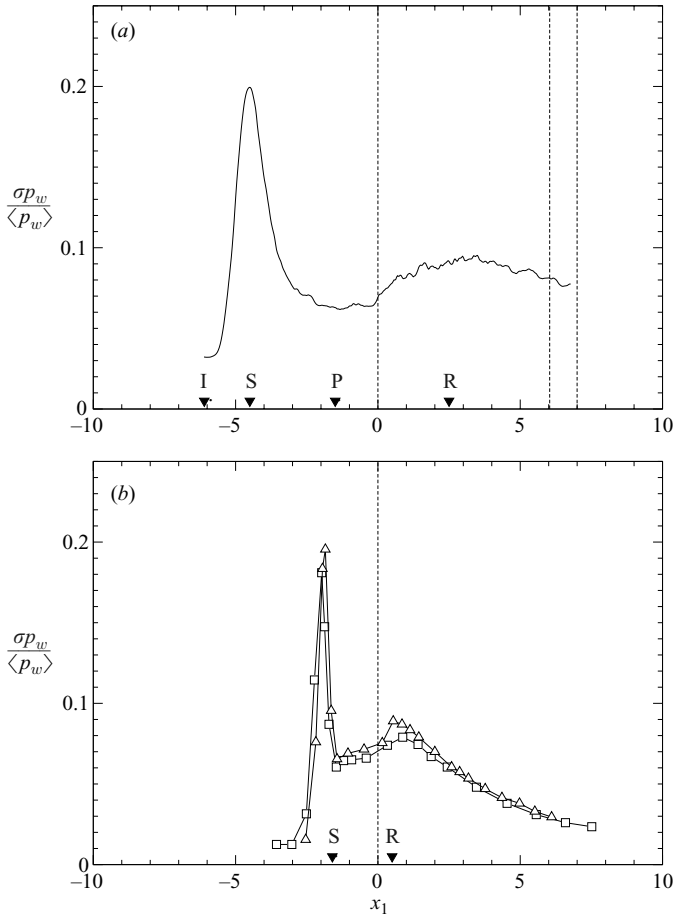


FIGURE 17. Standard deviation of wall pressure fluctuation: (*a*) computation and (*b*) experiment of Dolling & Murphy (1983). —□—, $Re_{\delta_0} = 780\,000$; —△—, $Re_{\delta_0} = 1\,400\,000$. Vertical lines have the same meaning as in figure 13.

Characteristic of the standard-deviation distribution is a second peak which can be found near the reattachment position. Its value is about 9 % of the local mean wall pressure for both computation and experiment.

4.3. *Turbulence evolution*

One of the most significant effects of shock–turbulence interaction is that turbulent fluctuations increase and turbulent length scales decrease when passing through sufficiently strong shocks. For a comprehensive summary of the current knowledge refer to Andreopoulos *et al.* (2000). For the case considered here, the amplification of turbulent fluctuations is evident from figure 18. Profiles of root-mean-square (RMS) values of the mass-flux $\langle(\rho U)'^2\rangle^{1/2}$, density $\langle\rho'^2\rangle^{1/2}$, and velocity $\langle U'^2\rangle^{1/2}$ fluctuations (*a–c*) are shown at several downstream sections as given in table 4. All quantities are normalized to the incoming free-stream quantities. The thick solid line denotes the time- and spanwise-averaged value, and the spanwise variation is indicated by dotted lines. Thin horizontal lines correspond to the location of zero mean velocity, which bounds the reverse flow region. The outer maxima which can be observed in sections 2–9 originate from unsteady shock motion as described in § 4.2. The maxima

https://doi.org/10.1017/S0022112006000930 Published online by Cambridge University Press

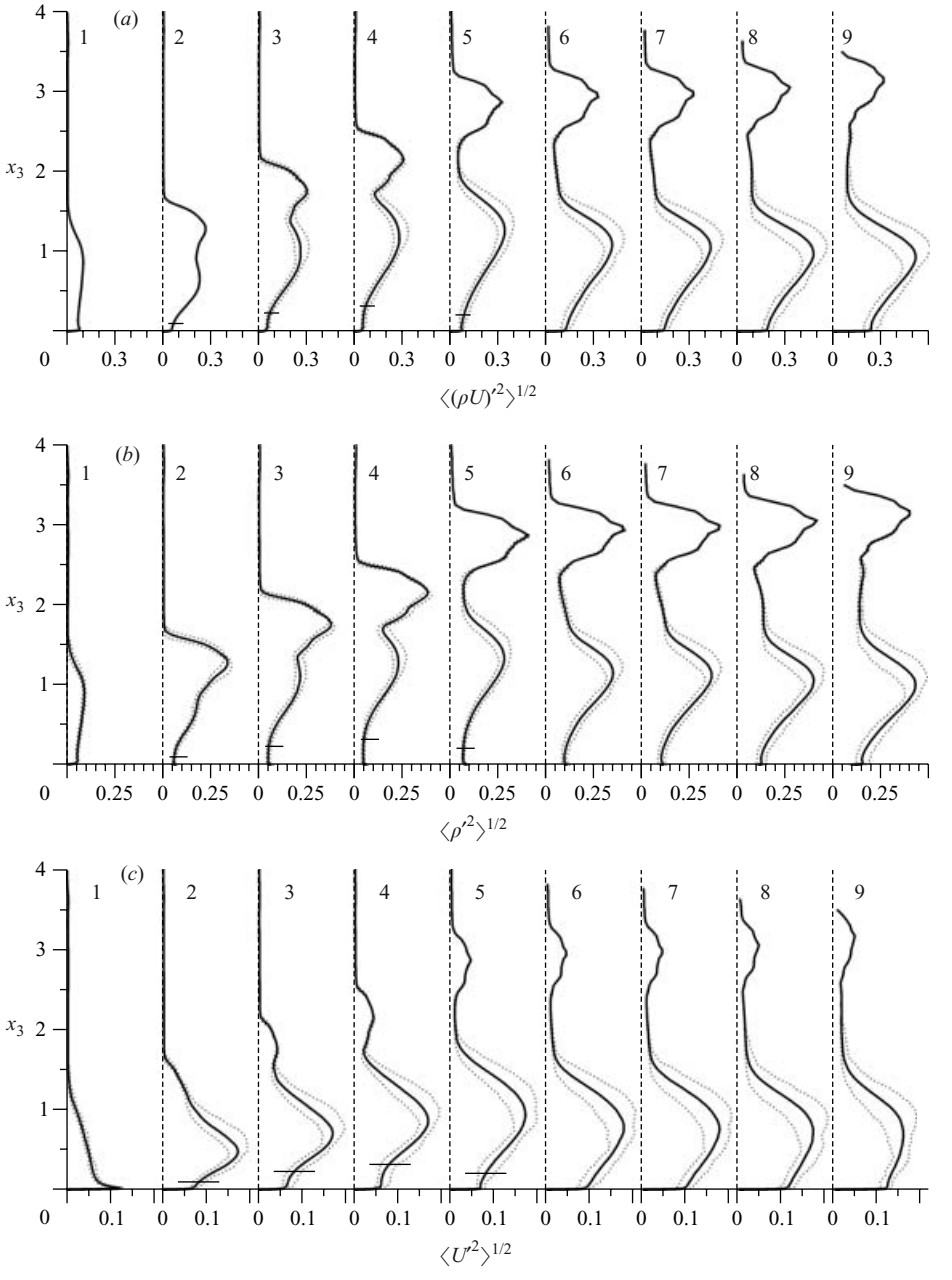


FIGURE 18. Downstream evolution of (*a*) mass-flux, (*b*) density and (*c*) velocity fluctuations. Positions are detailed in table 4.

between $x_3 = 0.75\delta_0$ and $x_3 = 1.25\delta_0$ are located within the deattached shear layer. The velocity fluctuations in the first section show the typical near-wall peak. Further downstream this peak remains but its fluctuation level is smaller than that of the detached shear layer. Whereas in the outer flow fluctuations are small at section 1, they grow by interaction with the shock wave (sections 5–9, $x_3 \approx 2.25$) up to values of larger than $0.1\rho_\infty$ for the density and about $0.01U_\infty$ for the velocity fluctuations.

https://doi.org/10.1017/S0022112006000930 Published online by Cambridge University Press

As mentioned before, aside from direct interaction with the shock wave, downstream travelling shocklets contribute additionally to this increase.

We compare data from RMS fluctuations with the reference experiment at positions E1 and E2 in figure 19. The measurement technique allowed only recording of relative changes of the RMS values where data of the undisturbed boundary layer serve as reference. We try to mimic the experimental procedure by normalizing our computational data with the respective maxima in the first section E1. Fluctuations of momentum and density are amplified by about a factor of 4 across the interaction, which agrees well with previous observations (Smits & Muck 1987; Adams 2000). The simulation shows larger amplifications than the experiment for all quantities near the local maxima in $0.7\delta_0 < x_3 < 1\delta_0$ at position E2, and for the density fluctuations in the external flow $x_3/\delta_0 > 1.5$. Given that the measurement error is at best between 15 % and 20 % the agreement between computational and experimental data nonetheless can be considered as satisfactory. Near-wall maxima of the RMS distributions are not captured by the experiment due to the lack of near-wall resolution. The streamwise behaviour of the momentum-fluctuation-profile maxima compares well with the reference experiment, figure 20.

The Reynolds normal stress $\tau_{11} = \langle \rho u_1^{c\prime\prime} u_1^{c\prime\prime} \rangle$, the Reynolds shear stress $\tau_{13} = \langle \rho u_1^{c\prime\prime} u_3^{c\prime\prime} \rangle$ and the structure parameter $-\tau_{13}/\tau_{ii}$ are shown using their contravariant repesentation in figures 21(a), 21(b) and 21(c), respectively. The Reynolds-normal-stress maximum is located near the wall in the incoming flow, shifts to the detached shear layer and diminishes at the last station. The amplification ratio of about 8 and the quantitative evolution are in agreement with those reported by Smits & Muck (1987) for a compression ramp with $\beta = 25^\circ$ at $M_\infty = 2.79$ and $Re_{\delta 0} = 1\,570\,000$. The Reynolds-shear-stress maxima (figure 21b) are amplified by factor of about 28, which is larger than that reported by Smits & Muck (1987). It was noted by Adams (2000) that τ_{13} is very sensitive to the the experimental probe adjustment. The spanwise variation reaches about ± 50 % in the calculation, while it was claimed that three-dimensional effects are small for experiments (Smits & Muck 1987).

Figure 21(a, b) indicates that Reynolds normal and shear stresses behave differently so that the turbulence structure changes. Anisotropy can be measured by the structure parameter, in figure 21(c). Its value of between 0.13 and 0.15 in the incoming boundary layer agrees well with data reported by Adams (2000) and with incompressible boundary layers (Smits & Dussauge 1996). Particularly large values can be observed in the detached shear layer.

4.4. *Development of the reverse flow*

As already mentioned in § 1 the reverse flow exhibits indications of relaminarization inside the separation zone. Zheltovodov (1979, 1996) found that a favourable pressure gradient acting on the reverse flow between the reattachment and separation lines and a decrease of the local Reynolds number can lead to a transformation of the reverse-flow velocity profiles from a shape which is typical for turbulent near-wall jets to a shape which is typical for laminar ones. RANS calculations for a 90° step with a $k-\omega$ turbulence model also revealed indications of this kind of transformation and a decrease of eddy viscosity in the revese flow ahead of a 90° step (Borisov *et al.* 1996). Bedarev *et al.* (1998) have demonstrated that it is possible to predict relaminarization in the separation regions for forward-facing steps and compression ramps through an *ad hoc* modification of ω. These computations indicate the importance of modelling this phenomenon for a better prediction of surface pressure, skin friction, and heat transfer in the separation regions for this purpose. A comparison of RANS

https://doi.org/10.1017/S0022112006000930 Published online by Cambridge University Press

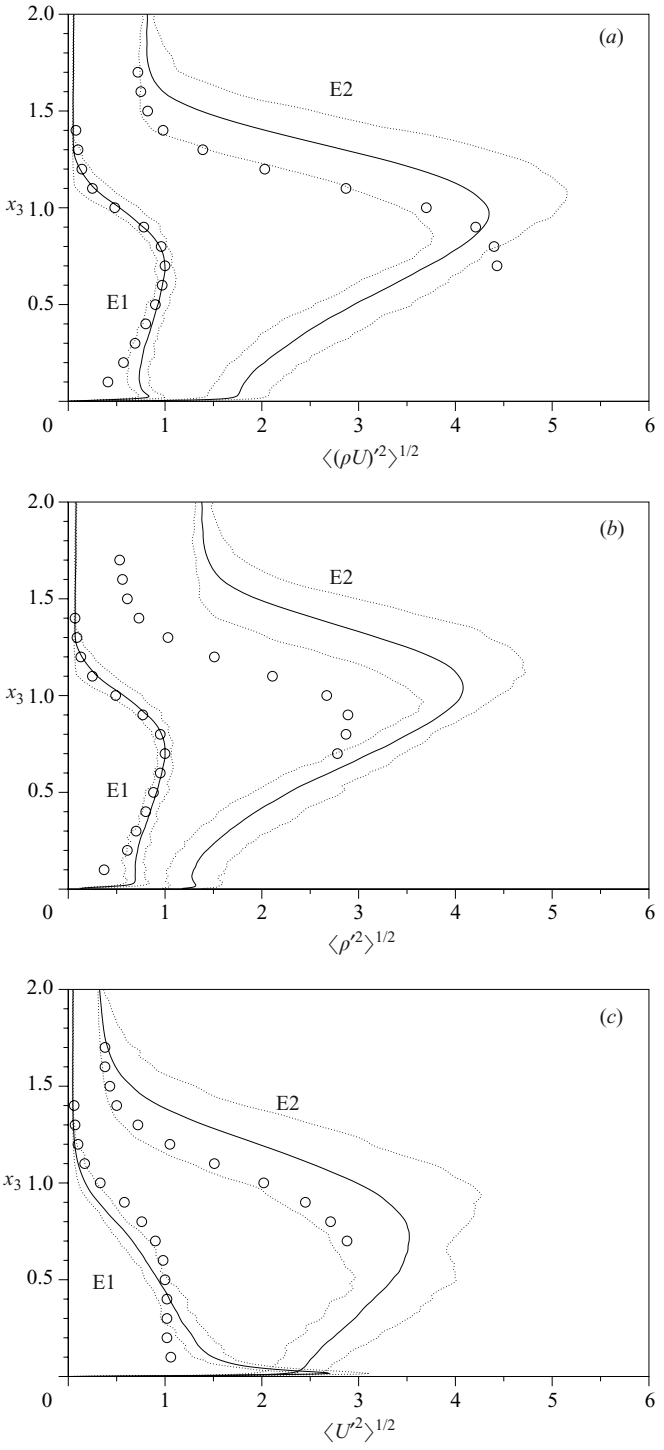


FIGURE 19. Amplification of RMS of (*a*) momentum, (*b*) density and (*c*) velocity fluctuations between position E1 and position E2. ○, reference experiment; ——, present LES averaged in time and over spanwise direction; ·····, present LES averaged in time, minimum and maximum values over the spanwise direction.

https://doi.org/10.1017/S0022112006000930 Published online by Cambridge University Press

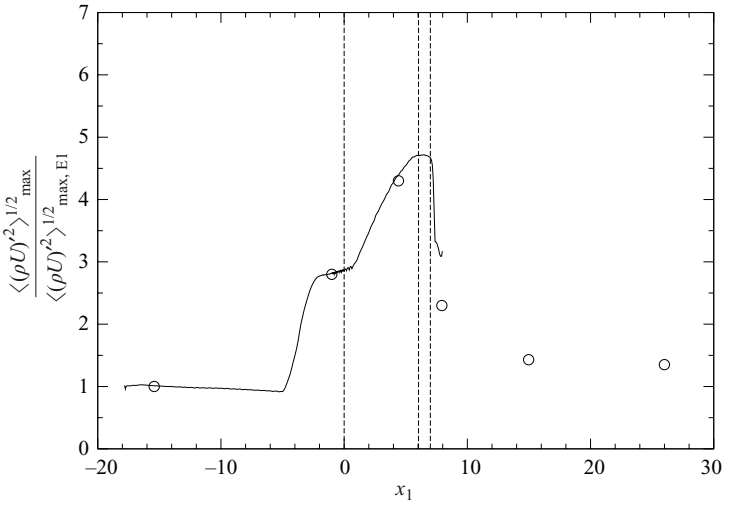


FIGURE 20. Relative changes of maximum RMS of momentum fluctuations with streamwise direction: ○, reference experiment; ——, present LES.

calculations with experimental data at $M_\infty = 3$ and a wide range of deflection angles of $\beta = 8°, 25°, 45°$ and $90°$ was performed by Zheltovodov (1996) and Borisov *et al.* (1999).

The mean velocity profiles for the separated region are plotted in figure 22. The reverse velocity is normalized to its maximum value $U_{\max}$; the wall-normal coordinate is normalized by $l_{1/2}$ where the mean velocity is half of its maximum value. In such variables a turbulent near-wall jet has a universal profile indicated by the thick solid line; the dashed line denotes a laminar profile (Vulis & Kashkarov 1965, p. 262). The higher-Reynolds-number experimental data at sections 3, 4 and 5 are shown in figure 22(*a*), and computational results at corresponding streamwise positions are shown in figure 22(*b*). It can be seen that the experimental profiles are scattered around laminar jet profile. The simulation exhibits a clear tendency of a transformation from turbulent to laminar jet profiles. This agrees with the experimental finding of Zheltovodov (1979) near a forward-facing $90°$ step.

Based on an analysis of mean-flow and turbulence measurements for a backward-facing step, Adams & Johnston (1988) found that a process similar to an inverse transition can also appear in subsonic turbulent separation. Following their suggestion we show the evolution of mean-flow profiles scaled in outer units (figure 23*a*) and in wall units (figure 23*b*). For reference, a $U/U_{\max} = (x_3/\delta_{\max})^{1/7}$ law and a log-law $U^+_{VD} = \ln x_3^+/0.4 + 5.1$ are shown additionally, where the boundary-layer thickness $\delta_{\max}$ here is defined as the wall-normal distance of the point of maximum reverse velocity. An evolution away from the turbulent shape is evident.

The variation of maximum negative velocity in the reverse flow $U_{\max}$ is shown in figure 24. From reattachment R to separation S the reverse flow accelerates strongly due to the favourable (negative) pressure gradient up to the corner position. From these data the acceleration parameter $(\nu/U^2_{\max})(\mathrm{d}U_{\max}/\mathrm{d}x)$, which is commonly used to assess the relaminarization conditions, can be estimated as between 10^{-4} and 4×10^{-4} which is in the same range as reported by Adams & Johnston (1988). It is two orders of magnitude larger than the relaminarization limit of 3.0×10^{-6} (Adams & Johnston 1988). This supports the possibility of relaminarization, which is also in

https://doi.org/10.1017/S0022112006000930 Published online by Cambridge University Press

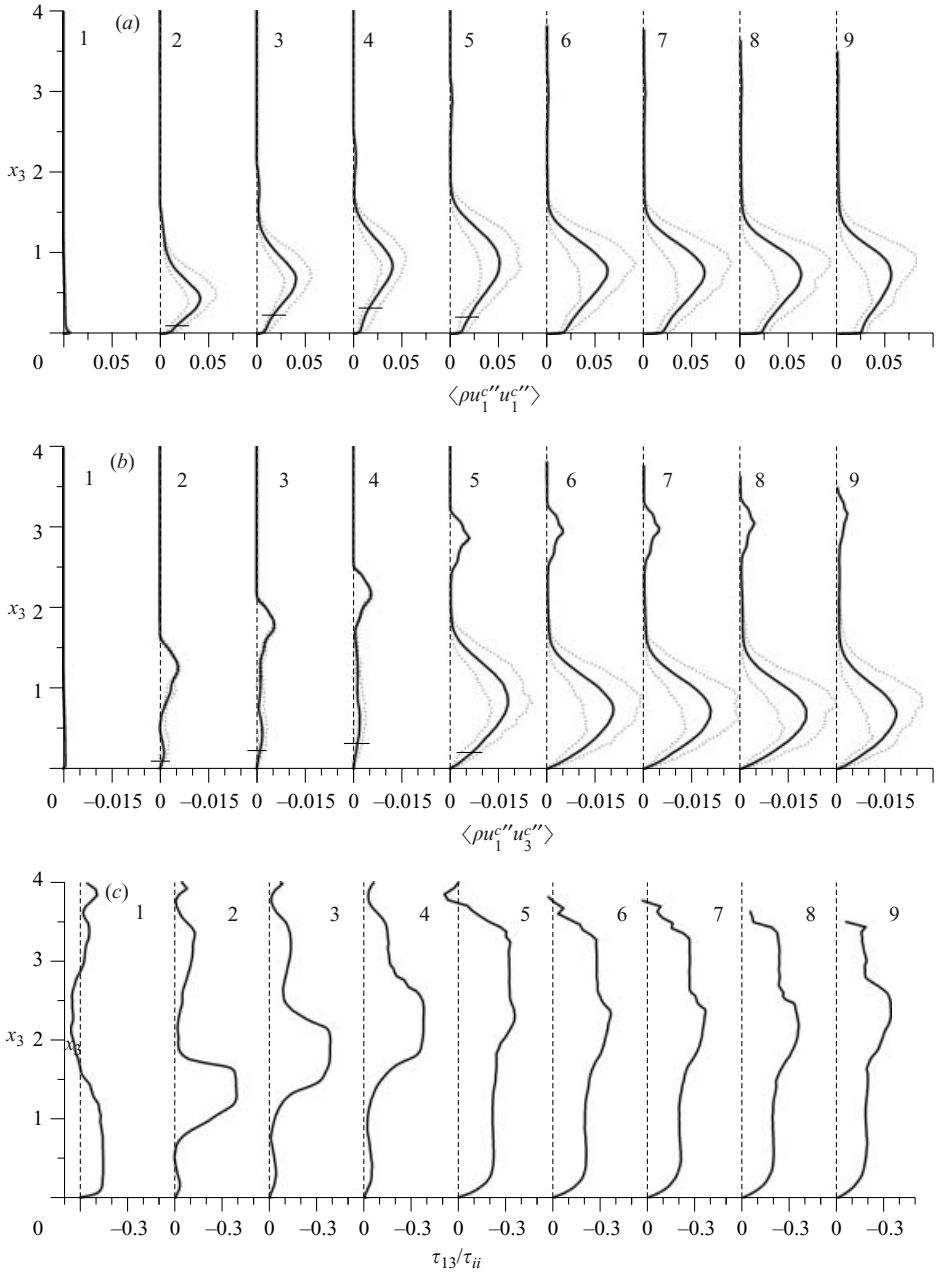


FIGURE 21. (*a*) Reynolds normal stress $\tau_{11} = \langle \rho u_1^{c\prime\prime} u_1^{c\prime\prime} \rangle$, (*b*) the Reynolds shear stress $\tau_{13} = \langle \rho u_1^{c\prime\prime} u_3^{c\prime\prime} \rangle$ and (*c*) the structure parameter $-\tau_{13}/\tau_{ii}$ at several downstream positions.

agreement with the decrease of velocity fluctuations along the line of maximum negative velocity, figure 24. After the corner the reverse flow slows down and the near-wall-jet mean-velocity profile assumes a laminar shape. A slight increase of velocity fluctuations can be attributed to its approaching the highly unsteady region near separation S.

https://doi.org/10.1017/S0022112006000930 Published online by Cambridge University Press

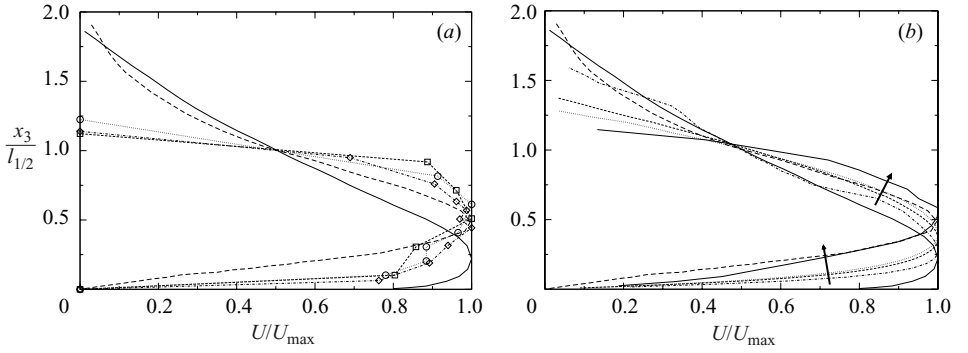


FIGURE 22. Mean velocity in the reverse flow plotted in wall-jet variables: (*a*) higher-Reynolds-number experiment and (*b*) current simulation ——, turbulent near-wall jet; – – – –, laminar near-wall jet; ○, section 3; □, section 4; ◇, section 5; ——, section 2; ·····, section 3; – – – –, section 4; —·—, section 5.

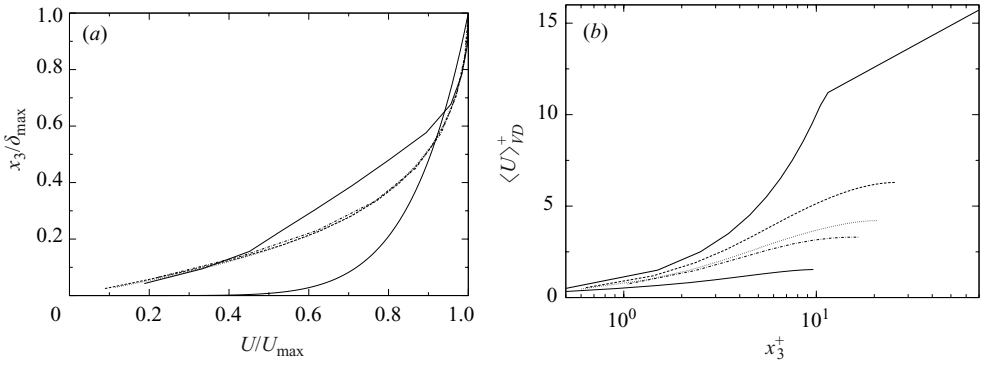


FIGURE 23. Mean velocity in the reverse flow plotted (*a*) in outer boundary layer scaling and (*b*) inner scaling: ——, section 2; ·····, section 3; – – – –, section 4; —·—, section 5. ——, power-law $U/U_{max} = (x_3/\delta_{max})^{1/7}$ and log-law $\ln x_3^+/0.4 + 5.1$.

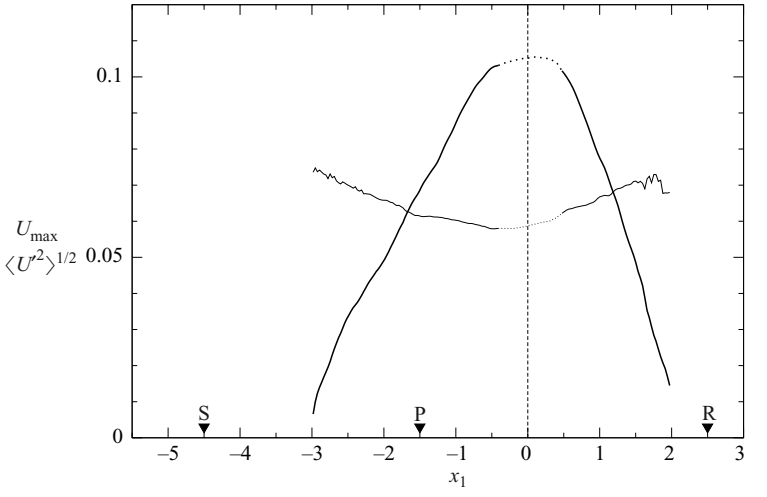


FIGURE 24. Maximum reverse velocity distribution and RMS of velocity fluctuations inside reverse flow: ——, U_{max}; ——, $\langle U'^2\rangle^{1/2}$ along U_{max}. The region around the corner where data were not analysed is indicated by a dotted line.

https://doi.org/10.1017/S0022112006000930 Published online by Cambridge University Press

5. Conclusions

A joint computational and experimental research effort has achieved a proper quantitative comparison between computation and experiment for a 25°-compression-ramp flow at a free-stream Mach number of $M_\infty = 2.95$ and a Reynolds number of $Re_{\delta_0} = 63\,560$. A correct prediction of the mean flow properties and unsteady flow phenomena was possible from a large-eddy simulation based on high-resolution numerical discretizations and the ADM approach for subgrid-scale modelling. In particular good agreement was achieved for surface-pressure and skin-friction distributions, mean velocity profiles, mass-flow, density and velocity fluctuations and wall-pressure-fluctuation distributions. It was possible to resolve the entire unsteady behaviour of the shock system around the separation region. Along with high-frequency fluctuations of the shock system a large-scale shock motion was confirmed by the simulation. Aside from direct shock–turbulence interaction a mechanism for turbulence amplification in the external flow above the detached shear layer was proposed based on downstream-travelling shocklets. This explains the nature of experimentally observed turbulence amplification and details its acoustic mode downstream of a shock wave. The existence of streamwise Görtler-type vortices was corroborated by simulation. The effect of these structures on the spanwise mean-flow variation should be taken into account in validation effords of CFD methods based on experimental data. Indications for a relaminarization tendency in the separation region were found.

This research was funded by the German Research Council (DFG) through grant AD 186/1. Computing time was granted by the German National Supercomputing Center in Stuttgart (HLRS).

REFERENCES

Adams, E. W. & Johnston, J. P. 1988 Flow structure in the near-wall zone of a turbulent separated flow. *AIAA J.* **26**, 932–939.

Adams, N. A. 1998 Direct numerical simulation of turbulent compression corner flow. *Theor. Comp. Fluid Dyn.* **12**, 109–129.

Adams, N. A. 2000 Direct simulation of the turbulent boundary layer along a compression ramp at $M = 3$ and $Re_\theta = 1685$. *J. Fluid Mech.* **420**, 47–83.

Adamson, T. C. & Messiter, A. F. 1980 Analysis of two-dimensional interactions between shock waves and boundary layers. *Annu. Rev. Fluid Mech.* **12**, 103–138.

Andreopoulos, J. & Muck, K. C. 1987 Some new aspects of the shock-wave/boundary-layer interaction in compression-ramp flows. *J. Fluid Mech.* **180**, 405–428.

Andreopoulos, Y., Agui, J. H. & Briassulis, G. 2000 Shock wave-turbulence interactions. *Annu. Rev. Fluid Mech.* **32**, 309–345.

Anyiwo, J. C. & Bushnell, D. M. 1982 Turbulence amplification in shock-wave boundary-layer interaction. *AIAA J.* **20**, 893–899.

Bedarev, I. A., Zheltovodov, A. A. & Fedorova, N. N. 1998 Supersonic turbulent separated flows numerical model verification. In *Intl Conf. on the Methods of Aerophysical Research, June 29–July 3, 1998, Part 1*, pp. 30–35. Novosibirsk, Russia.

Bertero, M. & Boccacci, P. 1998 *Introduction to Inverse Problems in Imaging*. Bristol: IOP Publishing.

Borisov, A. V., Vorontsov, S. S., Zheltovodov, A. A., Pavlov, A. A. & Shpak, S. I. 1993 Development of experimental and computational methods of studies of supersonic separated flows. Preprint 9–93 ITAM, RAS SB, Novosibirsk (in Russian).

Borisov, A. V., Zheltovodov, A. A., Maksimov, A. I., Fedorova, N. N. & Shpak, S. I. 1996 Verification of turbulence models and computational methods of supersonic separated flows.

https://doi.org/10.1017/S0022112006000930 Published online by Cambridge University Press

In *Intl Conf. on the Methods of Aerophysical Research, September 2–6, 1996, Part 1*, pp. 54–61. Novosibirsk, Russia.

Borisov, A. V., Zheltovodov, A. A., Maksimov, A. I., Fedorova, N. N. & Shpak, S. I. 1999 Experimental and numerical study of supersonic turbulent separated flows in the neighborhood of two-dimensional obstacles. *Mekh. Zhid. i Gaza* **2**, 26–37 (in Russian).

Bradshaw, P. 1977 Compressible turbulent shear layers. *Annu. Rev. Fluid Mech.* **9**, 33–54.

Brazhko, V. N. 1979 Periodic structure of the flow and heat transfer in the reattachment region of supersonic flow. *Uchenye Zapiski TsAGI* **10**, 113–118 (in Russian).

Chapman, D., Kuehn, D. & Larson, H. 1957 Investigation of separated flows in supersonic and subsonic streams with emphasis on the effect of transition. *Tech. Rep.* 1356. NACA.

Comte, P. & David, E. 1996 Large-eddy simulation of Görtler vortices in a curved compression ramp. In *Experimentation, Modelling and Computation in Flow, Turbulence and Combustion, vol. 1* (ed. J. A. Désidéi, B. N. Chetverushkin, Y. A. Kuznetsov, J. Périaux & B. Stoufflet), pp. 45–61. John Wiley and Sons.

Delery, J. & Marvin, J. 1986 Turbulent shock-wave/boundary layer interaction. *Tech. Rep.* AR–280. AGARD.

Dolling, D. S. 1998 High-speed turbulent seaparated flows: consistency of mathematic models and flow physics. *AIAA J.* **36**, 725–732.

Dolling, D. S. 2001 Fifty years of shock-wave/boundary-layer interaction research: What next? *AIAA J.* **39**, 1517–1531.

Dolling, D. S. & Murphy, M. T. 1983 Unsteadiness of the separation shock wave structure in a supersonic compression ramp flowfield. *AIAA J.* **12**, 1628–1634.

Dolling, D. S. & Or, C. T. 1985 Unsteadiness of the shock wave structure in attached and separated compression ramp flows. *Exps. Fluids* **3**, 24–32.

El-Askary, W. A., Schröder, W. & Meinke, M. 2003 LES of compressible wall-bounded flows. *AIAA Paper* 03-3554.

Erdos, J. & Pallone, A. 1962 *Shock-Boundary Layer Interaction and Flow Separation.* Stanford University Press.

Fernholz, H. H. & Finley, P. J. 1977 A critical compilation of compressible turbulent boundary layer data. *AGARDograph* 223. AGARD.

Fernholz, H. H. & Finley, P. J. 1981 A further compilation of compressible boundary layer data with a survey of turbulence data. *AGARDograph* 263. AGARD.

Floryan, J. M. 1991 On the Görtler instability of boundary layers. *Prog. Aerospace Sci.* **28**, 235–271.

Görtler, H. 1954 On the three-dimensional instability of laminar boundary layers on concave walls. *Tech. Rep.* 1375. NACA.

Hagemann, G., Frey M. & Koschel, W. Appearance of restricted shock separation in rocket nozzles, *J. Prop. Power* **3**, 557–584.

Hopkins, E. J. & Inouye, M. 1971 An evaluation of theories for predicting turbulent skin friction and heat transfer on flat plates at supersonic and hypersonic Mach numbers. *AIAA J.* **9**, 993–1003.

Hunt, D. L. & Nixon, D. 1995 A very large eddy simulation of an unsteady shock wave/turbulent boundary layer interaction. *AIAA Paper* 95-2212.

Inger, G. R. 1977 Three-dimensional heat- and mass- transfer effects across high-speed reattaching flows. *AIAA J.* **15**, 383–389.

Kannepalli, C., Arunajatesan, S. & Dash, S. M. 2002 RANS/LES methodology for supersonic transverse jet interactions with approach flow. *AIAA Paper* 02-1139.

Knight, D. D. & Degrez, G. 1998 Shock wave boundary layer interactions in high mach number flows – a critical survey of current CFD prediction capabilities. *Tech. Rep.* AR–319. AGARD.

Knight, D. D., Yan, H., Panaras, A. G. & Zheltovodov, A. A. 2003 Advances in CFD prediction of shock wave turbulent boundary layer interactions. *Prog. Aerospace Sci.* **39**, 121–184.

Kovasznay, L. S. G. 1953 Turbulence in supersonic flow. *J. Aero. Sci.* **20**, 657–682.

Lee, S., Lele, S. K. & Moin, P. 1991 Eddy shocklets in decaying compressible turbulence. *Phys. Fluids* A **3**, 657–664.

Lele, S. K. 1992 Compact Finite Difference Schemes with Spectral-like Resolution. *J. Comput. Phys.* **103**, 16–42.

https://doi.org/10.1017/S0022112006000930 Published online by Cambridge University Press

Loginov, M. S., Adams, N. A. & Zheltovodov, A. A. 2004*a* Large-eddy simulation of turbulent boundary layer interaction with successive shock and expansion waves. In *Intl Conf. on the Methods of Aerophysical Research, June 28–July 3, 2004, Part 1*, pp. 149–157. Novosibirsk, Russia.

Loginov, M. S., Adams, N. A. & Zheltovodov, A. A. 2004*b* LES of shock wave/turbulent boundary layer interaction. In *High Performance Computing in Science and Engineering 04* (ed. E. Krause, W. Jäger & M. Resch), pp. 177–188.

Lüdeke, H., Radespiel, R. & Schülein, E. 2004 Simulation of streamwise vortices at the flaps of re-entry vehicles. *Aerospace Sci. Tech.* **8**, 703–714.

Lund, T. S., Wu, X. & Squires, K. D. 1998 Generation of turbulent inflow data for spatially-developing boundary layer simulations. *J. Comput. Phys.* **140**, 233–258.

Rizzetta, D. P. & Visbal, M. R. 2002 Application of large-eddy simulation to supersonic compression ramps. *AIAA J.* **40**, 1574–1581.

Rizzetta, D. P., Visbal, M. R. & Gaitonde, D. V. 2001 Large-eddy simulation of supersonic compression-ramp flow by high-order method. *AIAA J.* **39**, 2283–2292.

Sagaut, P. 2002 *Large-Eddy Simulation for Incompressible Flows*, 2nd edn. Springer.

Settles, G. S. & Dodson, L. J. 1991 Hypersonic shock/boundary-layer interaction database. *NASA CR* 177577. NASA Ames Research Center, Moffet Field, California.

Settles, G. S. & Dodson, L. J. 1994 Supersonic and hypersonic shock/boundary layer interaction database. *AIAA J.* **32**, 1377–1383.

Settles, G. S. & Dolling, D. S. 1990 Swept shock/boundary-layer interactions — tutorial and update. *AIAA Paper* 90-0375.

Settles, G. S., Fitzpatrick, T. J. & Bogdonoff, S. M. 1979 Detailed study of attached and separated compression corner flowfields in high Reynolds number supersonic flow. *AIAA J.* **17**, 579–585.

Smits, A. J. & Dussauge, J.-P. 1996 *Turbulent Shear Layers in Supersonic Flow*. AIP Press.

Smits, A. J. & Muck, K.-C. 1987 Experimental study of three shock wave/turbulent boundary layer interactions. *J. Fluid Mech.* **182**, 291–314.

Spalart, P. R. 1988*a* Direct simulation of a turbulent boundary layer up to $Re_\theta = 1410$. *J. Fluid Mech.* **187**, 61–98.

Spalart, P. R. 1988*b* Direct simulation of a turbulent boundary layer up to $Re_\theta = 1410$. *J. Fluid Mech.* **187**, 61–98.

Stolz, S. & Adams, N. A. 2003 Large-eddy simulation of high-Reynolds-number supersonic boundary layers using the approximate deconvolution model and a rescaling and recycling technique. *Phys. Fluids* **15**, 2398–2412.

Stolz, S., Adams, N. A. & Kleiser, L. 2001*a* The approximate deconvolution model for large-eddy simulation of compressible flows and its application to shock-turbulent-boundary-layer interaction. *Phys. Fluids* **13**, 2985–3001.

Stolz, S., Adams, N. A. & Kleiser, L. 2001*b* An approximate deconvolution model for large-eddy simulation with application to incompressible wall-bounded flows. *Phys. Fluids* **13**, 997–1015.

Urbin, G., Knight, D. & Zheltovodov, A. A. 1999 Compressible large eddy simulation using unstructured grid – supersonic turbulent boundary layer and compression corner. *AIAA Paper* 99-0427.

Urbin, G., Knight, D. & Zheltovodov, A. A. 2000 Large eddy simulation of a supersonic compression corner. *AIAA Paper* 00-0398.

Vulis, L. A. & Kashkarov, W. P. 1965 *Theory of the Viscous Liquid Jets*. Moscow: Nauka (in Russian).

Williamson, J. H. 1980 Low-storage Runge-Kutta schemes. *J. Comput. Phys.* **35**, 48–56.

Wu, M., Bookey, P., Martin, M. P. & Smits, A. J. 2005*a* Analysis of shockwave/turbulent boundary layer interaction using DNS and experimental data. *AIAA Paper* 05-310.

Wu, M. & Martin, M. P. 2006 Assessment of numerical methods for DNS of shockwave/turbulent boundary layer interaction. *AIAA Paper* 06-0717.

Wu, M., Taylor, E. M. & Martin, M. P. 2005*b* Assessment of STBLI DNS data and comparison against experiments. *AIAA Paper* 05-4895.

Yan, H., Knight, D. & Zheltovodov, A. A. 2001 Large eddy simulation of supersonic compression corner using ENO scheme. In *Third AFOSR Intl Conf. on DNS and LES, August 5–9, 2001,* pp. 381–388. Arlington: Univ. of Texas.

https://doi.org/10.1017/S0022112006000930 Published online by Cambridge University Press

Yan, H., Urbin, G., Knight, D. & Zheltovodov, A. A. 2000 Compressible large eddy simulation using unstructured grid: supersonic boundary layers and compression ramps. In *Intl Conf. on the Methods of Aerophysical Research, 9–14 July, 2000, Part 1*, pp. 215–224. Novosibirsk, Russia.

Zheltovodov, A. A. 1979 Analysis of properties of two-dimensional separated flows at supersonic speeds conditions. In *Investigations of Near-wall Flows of Viscous Gas* (ed. N. N. Yanenko), pp. 59–94. Novosibirsk: Institute of Theoretical and Applied Mechanics, USSR Academy of Sciences (in Russian).

Zheltovodov, A. A. 1991 Peculiarities of development and modeling possibilities of supersonic turbulent separated flows. In *Separated Flows and Jets: IUTAM Symposium, July 9–13, 1990* (ed. V. V. Kozlov & A. V. Dovgal), pp. 225–236. Novosibirsk, USSR.

Zheltovodov, A. A. 1996 Shock waves/turbulent boundary-layer interactions – fundamental studies and applications. *AIAA Paper* 96-1977.

Zheltovodov, A. A. 2004 Advances and problems in modelling of shock wave turbulent boundary layer interactions. In *Intl Conf. on the Methods of Aerophysical Research, Part 2, June 28–July 3, 2004*, pp. 149–157. Novosibirsk, Russia.

Zheltovodov, A. A., Borisov, A. V., Knight, D. D., Horstman, C. C. & Settles, G. S. 1992 The possibilies of numerical simulation of shock waves/boundary layer interaction in supersonic and hypersonic flows. In *Intl Conf. on the Methods of Aerophysical Research, Part 1, August 31–September 4, 1992*, pp. 164–170. Novosibirsk, Russia.

Zheltovodov, A. A., Schülein, E. & Yakovlev, V. N. 1983 Development of turbulent boundary layer under conditions of mixed interaction with shock and expansion waves. Preprint 28–83 ITAM, USSR Academy of Sciences, Siberian Branch, Novosibirsk (in Russian).

Zheltovodov, A. A., Trofimov, V. M., Schülein, E. & Yakovlev, V. N. 1990 An experimental documentation of supersonic turbulent flows in the vicinity of forward- and backward-facing ramps. *Tech. Rep.* 2030. Institute of Theoretical and Applied Mechanics, USSR Academy of Sciences, Novosibirsk.

Zheltovodov, A. A. & Yakovlev, V. N. 1986 Stages of development, flowfield structure and turbulence characteristics of compressible separated flows in the vicinity of 2-D obstacles. Preprint 27–86 ITAM, USSR Academy of Sciences, Siberian Branch, Novosibirsk (in Russian).

https://doi.org/10.1017/S0022112006000930 Published online by Cambridge University Press